

Annual Review of Condensed Matter Physics
**Smart Responsive Polymers:
Fundamentals and Design
Principles**

Debashish Mukherji,^{1,2} Carlos M. Marques,³
and Kurt Kremer²

¹Stewart Blusson Quantum Matter Institute, University of British Columbia, Vancouver, British Columbia V6T 1Z4, Canada; email: debashish.mukherji@ubc.ca

²Max-Planck-Institut für Polymerforschung, 55128 Mainz, Germany; email: mukherji@mpip-mainz.mpg.de, kremer@mpip-mainz.mpg.de

³Institut Charles Sadron, Université de Strasbourg, CNRS, 67034 Strasbourg, Cedex 2, France; email: marques@unistra.fr

Annu. Rev. Condens. Matter Phys. 2020. 11:271–99

First published as a Review in Advance on
December 3, 2019

The *Annual Review of Condensed Matter Physics* is
online at conmatphys.annualreviews.org

<https://doi.org/10.1146/annurev-conmatphys-031119-050618>

Copyright © 2020 by Annual Reviews.
All rights reserved

Keywords

soft matter, smart polymers, multiresponsive systems, solvation
thermodynamics

Abstract

In this review, we summarize recent theoretical and computational developments in the field of smart responsive materials, together with complementary experimental data. A material is referred to as smart responsive when a slight change in external stimulus can drastically alter its structure, function, or stability. Because of this smart responsiveness, these systems are used for the design of advanced functional materials. The most characteristic properties of smart polymers are discussed, especially polymer properties in solvent mixtures. We show how multiscale simulation approaches can shed light on the intriguing experimental observations. Special emphasis is given to two symmetric phenomena: co-non-solvency and co-solvency. The first phenomenon is associated with the collapse of polymers in two miscible good solvents, whereas the latter is associated with the swelling of polymers in poor solvent mixtures. Furthermore, we discuss when the standard Flory–Huggins-type mean-field polymer theory can (or cannot) be applied to understand these complex solution properties. We also sketch a few examples to highlight possible future directions, that is, how smart polymer properties can be used for the design principles of advanced functional materials.

ANNUAL
REVIEWS **CONNECT**

www.annualreviews.org

- Download figures
- Navigate cited references
- Keyword search
- Explore related articles
- Share via email or social media

1. INTRODUCTION

Soft, smart, and small are three keywords that are essential in designing multiresponsive materials for advanced functional applications (1–6). A material is referred to as smart responsive when a slight change in external stimulus can drastically alter its structure, function, or stability. These stimuli can be temperature (7–14), ionic strength (13, 15–17), cosolvent composition (18–36), light (36–42), and mechanical stress (43–45), to name a few. Furthermore, when the relevant energy scale in the systems is of the order of the thermal energy $k_B T$, the materials are classified as soft matter and, thus, are dictated by large conformational and compositional fluctuations. Because of these strong fluctuations, entropy (generic physical concepts and scaling laws) becomes as important as energy (molecular level chemical details). Therefore, establishing a delicate balance between entropy and energy is at the heart of understanding soft matter properties.

Polymers are one class of soft materials that are of high importance as they provide a suitable platform to tune materials properties while still having rather simple materials processing. For example, establishing the microscopic understanding of the solvation behavior of smart polymeric materials, such as hydrogels, microgels, and/or composite networks in single or multicomponent solvents, is of tremendous technological interest. This ranges from organic semiconductors (46), photonic band gap materials (47–50), self-healing networks (51–53), tuning of thermal conductivity of thermoplastic materials (54, 55), and biomedical applications (56–62), to name a few.

In this review, we highlight recent developments in the field of smart responsive polymers and their connections to the design of soft materials. We discuss recent experimental findings and show how complementary molecular simulation data, together with theoretical arguments, can shed light to better understand polymer properties in aqueous and aqueous cosolvent mixtures. In this context, it is important to note that polymer properties are inherently multiscale in nature, where delicate local interaction details play a key role in describing the large-scale conformational properties. We therefore emphasize the need for multiscale modeling to arrive at a comprehensive view of the existing experimental findings. We also discuss open questions in this field.

2. THERMORESPONSIVE SMART POLYMERS

Most commonly known smart polymers are those that swiftly change their conformation upon varying temperature T , thus they are also known as thermoresponsive smart polymers. Here, T responsiveness can be classified as either lower critical solution (LCST) or upper critical solution (UCST) behavior. In the case of LCST, monomer–solvent interactions confer an expanded polymer structure at low T . When T is increased above a certain critical value T_c , monomer–solvent interaction becomes significantly weaker and, thus, solvent molecules get expelled from near the polymer backbone. In this process, the energy–entropy balance is such that the translational entropy of the released solvent molecules wins; i.e., solvent translational entropy becomes larger than the polymer conformational entropy loss upon collapse. Because a chain collapses upon increasing T , LCST transition is an entropy-driven process as already proposed by Flory (63–65). In this case, T_c is referred to as T_ℓ , the lower critical solution temperature of a polymer in a particular solvent. For microgels, $T_\ell = T_{VPTT}$ with T_{VPTT} being the volume phase transition temperature (66–68). Typical examples of LCST systems are those that are mostly governed by hydrogen bonding between monomer and solvent molecules, where the solvent (or one of the solvents) is usually water. However, when a polymer undergoes globule-to-coil transition upon increase of T , this is referred to as UCST transition and is an energy-driven process.

In a standard LCST collapse, starting from a good solvent condition (for $T < T_\ell$), increasing the effective attraction between monomers first brings a polymer into a Θ condition in which the short-range excluded-volume repulsion is exactly canceled by the long-range attraction. Further

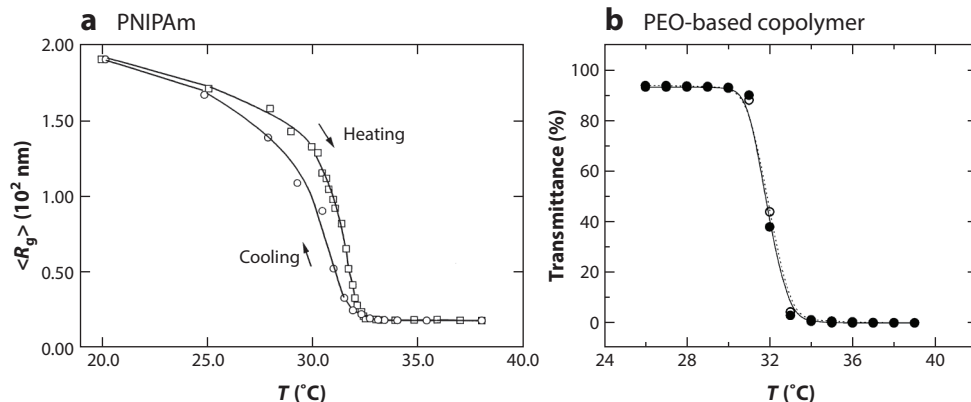


Figure 1

(a) Gyration radius R_g of a poly(*N*-isopropylacrylamide) chain in water. The transition temperature is around 32°C (or 305 K). A hysteresis is observed between the heating and cooling cycles around this transition temperature. (b) Turbidity measurement of a semidilute solution of a poly(ethyleneoxide)-based system. The transition temperature is around 32°C (or 305 K), with no hysteresis observed around transition temperature. Abbreviations: PEO, poly(ethylene oxide); PNIPAm, poly(*N*-isopropylacrylamide). Panel *a* adapted with permission from *Macromolecules* 31, 2972; Copyright 1998 American Chemical Society, and panel *b* is adapted with permission from *Macromolecules* 49, 1858; Copyright 2016 American Chemical Society.

increase of monomer–monomer attraction collapses a polymer into a compact globule. This globular conformation is controlled by a balance between the second virial osmotic contributions with attractive coefficient $-\lvert\mathcal{V}\rvert$ and three body repulsions, where \mathcal{V} is the monomer-excluded volume. In the Θ collapse is a second-order phase behavior, with the critical point (or the Θ point) characterized by large diverging fluctuations. In some cases a hysteresis is also observed near T_ℓ , indicating a first-order-like transition, and thus is represented by a bimodal distribution in the interaction energy (69, 70). It should also be mentioned that a hysteresis is usually visible for polymers with short side groups, such as the poly(*N*-isopropylacrylamide) (PNIPAm; 7, 8) and poly(*N*-*n*-propylacrylamide) (PNNIPAm; 71, 72). By contrast, linear chains (such as PEO, i.e., poly(ethyleneoxide), or PEO-based systems) do not show any hysteresis (see **Figure 1b** for more details; 13). Therefore, the specific correlation between the monomer-level structural packing and first- or second-order-like transitions for LCST systems is still not entirely understood.

For a given chemical structure of monomer species in a homopolymer chain, T_ℓ is rather well defined. For example, an atactic PNIPAm chain has a $T_\ell \sim 305\text{ K}$ (7), which can be tuned by changing monomer-level chemistry. Here, an increase in hydrophobicity, as seen by changing the isopropyl group to *n*-propyl, leads to a reduced $T_\ell \sim 297\text{ K}$ (71, 72). However, adding an extra methyl group to the backbone alkane chain of PNIPAm, as in the case of poly(*N*-isopropylmethacrylamide) (PNIPMAM; 73), T_ℓ increases to $\sim 313\text{ K}$. Additional methyl group is expected to increase hydrophobicity and thus should ideally reduce T_ℓ . Here, however, an opposite trend is observed. Therefore, slight changes in monomer structures can cause unexpected changes of the polymer properties and lead to noticeably different T_ℓ values.

T_ℓ can also be tuned by changing the tacticity of a polymer chain. For example, going from a chain with 100% meso dyads (isotactic chain) to 0% meso dyads or 100% racemo dyads (syndiotactic chain), T_ℓ follows the trend $T_\ell^{\text{isotactic}} < T_\ell^{\text{atactic}} < T_\ell^{\text{syndiotactic}}$ with a 50–50 combination of meso and racemo dyads approximately corresponding to an atactic chain (74–76). Here, the

stiffness of a chain, as measured in terms of the Kuhn length ℓ_k , follows the trend $\ell_k^{\text{isotactic}} < \ell_k^{\text{atactic}} < \ell_k^{\text{syndiotactic}}$ (76). Following simple entropic arguments, the stiffer the chain, the lesser its solubility. This will then correspond to decreasing LCST with increasing ℓ_k . However, we observe an opposite trend; that is, a chain becomes stiffer yet it is better soluble in water. This unexpected behavior can be attributed to the different solvation structures around the side groups that are more exposed when a chain has syndiotacticity. Another possible route to tune T_ℓ is by copolymerization. This is discussed in the following section.

2.1. Effect of Copolymer Sequence

A more flexible tuning of T_ℓ can be achieved by introducing hydrophilic (or hydrophobic) monomers along the native polymer backbone, where a larger hydrophilicity (or hydrophobicity) is described in comparison with the native homopolymer chain. More specifically, introducing hydrophilic units usually increases T_ℓ , whereas hydrophobic units decrease T_ℓ . An example includes copolymer sequence poly(NIPAm-co-Am) consisting of two monomers: acrylamide (Am) and N-isopropylacrylamide (NIPAm; 77, 78). It should be noted that Am is more hydrophilic than NIPAm, where no T_ℓ is reported within the range of 273–350 K in pure water. Therefore, as expected, increasing Am monomer mole fraction x_a along a PNIPAm backbone also increases T_ℓ (see a comparative simulation and experimental plot in **Figure 2**; 76–78). Furthermore, for p(NIPAm-co-Am), the increase in T_ℓ is difficult to predict and displays a nonlinear variation with increasing x_a . Therefore, it is desirable to have a more predictive and tunable polymer sequence. In this context, copolymer sequences consisting of hydrophobic (methylene) and hydrophilic (ethylene-oxide) monomer units (see **Figure 3a,b**) were recently synthesized (13), which show highly predictive thermal responsiveness. An added advantage of these systems is that they are acetal linked, making them pH degradable (13). Note that the covalent carbon–carbon bonds are very strong, and long chains are nonbiodegradable, leading to severe environmental problems. Adding acetal linkages along the backbone makes such polymers biodegradable and highly suitable

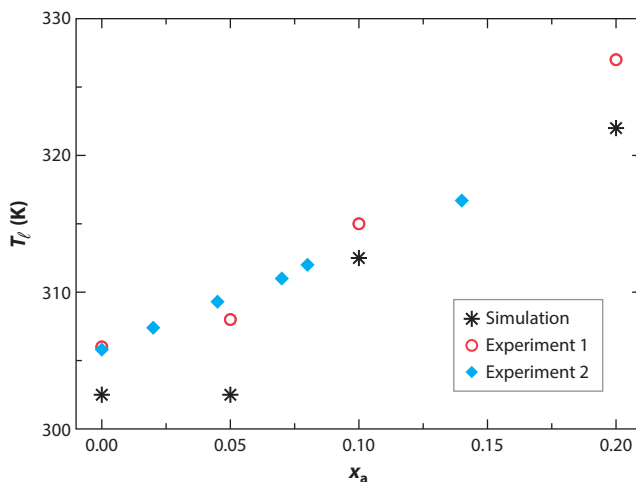


Figure 2

Lower critical solution temperature T_ℓ of a random copolymer of poly(N-isopropylacrylamide) and poly(N-isopropylacrylamide) as a function of acrylamide mole fraction x_a . Figure adapted with permission from *Journal of Chemical Physics* 146, 034904; Copyright 2017 American Institute of Physics.

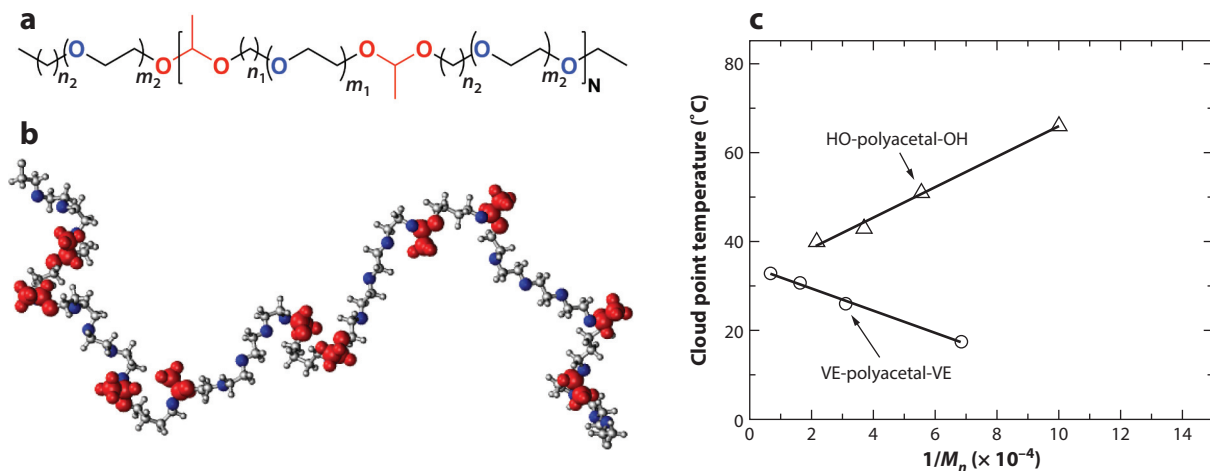


Figure 3

(a) The chemical structure and (b) a simulation snapshot of a polyacetal chain. Here, the hydrophobic methylene units (represented by n_1 and n_2) and hydrophilic ethylene oxide units (represented by m_1 and m_2) are tuned to obtain different amphiphilic sequences. Panel c presents a Flory–Fox relationship showing transition temperature with inverse of the molecular weight M_n for a given copolymer sequence. Panels a and b adapted with permission from *Journal of Chemical Physics* 147, 064904; Copyright 2017 American Institute of Physics, and panel c adapted with permission from *Macromolecules* 49, 1858; Copyright 2016 American Chemical Society.

for biocompatible applications. In polyacetal, as it is named in Reference 13, increasing the fractions of hydrophobic (represented by n_i) or hydrophilic (represented by m_i) units (see **Figure 3a**) linearly changes T_ℓ of copolymer chains. Because of this linear behavior, which was also observed in a generic molecular simulation study of amphiphilic copolymers (79), these copolymer sequences provide a rather flexible molecular toolbox for desired applications. Importantly, these systems also show severe chain length effects. As shown in **Figure 3c**, a molecular weight M_n of above 10^4 g/mol is required to obtain a well-converged cloud point temperature T_{cp}^∞ . In addition, depending on hydrophilic (-OH) or hydrophobic (vinyl ester -VE) termination, T_{cp} shows different signs in their slopes with M_n , with both following the Flory–Fox relationship (63–65),

$$T_{cp} = T_{cp}^\infty - \frac{\text{const.}}{M_n}. \quad 1.$$

Furthermore, as indicated by **Figure 3c**, specific chemical details are only important for rather short chain lengths (or oligomeric units), and the polymer behavior in the asymptotic limit is independent of their end terminations. In this asymptotic limit the (co-)polymer structures are described by the statistical distribution of polymer segments, whereas the global polymer conformation is well described by scaling laws.

2.2. Systematic Structural Coarse-Graining of Polymer Solution

Although polyacetal-based systems are highly important for smart materials design, a broader applicability and/or usefulness will also require predictive design principle of a rather large set of polymer architectures. This, however, is not at all trivial in experiments. Computer simulations, especially coarse-grained (CG) models, are extremely important in understanding, interpreting and guiding experiments into new directions. Therefore, CG models have been developed to study these systems (80). In this context, a linear dependence of T_{cp} with polymer sequences, as seen from

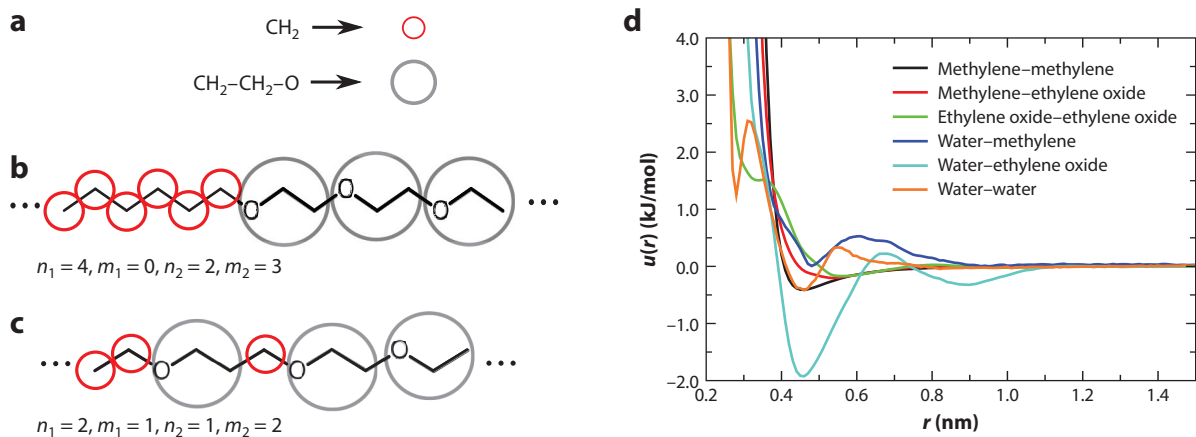


Figure 4

Mapping schemes of (a) methylene and ethylene oxide monomers and two different copolymer sequences, namely (b) $n_1 = 4$, $m_1 = 0$, $n_2 = 2$, and $m_2 = 3$ and (c) $n_1 = 2$, $m_1 = 1$, $n_2 = 1$, and $m_2 = 2$, respectively. Panel d shows the pair-wise coarse-grained potentials. Figure adapted with permission from *Journal of Chemical Physics* 147, 064904; Copyright 2017 American Institute of Physics.

the experiments (13), indicates that there is no cross-correlation between effects because of two monomer types. Therefore, a systematic CG model was developed at the segment (or monomer) level. A simple mapping scheme is shown in **Figure 4a**, with two corresponding copolymer sequences in **Figure 4b,c**. For the derivation of the CG model a combination of two structure-based techniques for solutions was used (81, 82), namely the iterative Boltzmann inversion (IBI; 83) and the cumulative iterative Boltzmann inversion (C-IBI; 84). In a nutshell, the IBI procedure starts from an initial guess of the interaction potential of the CG model $V_0(r) = -k_B T \ln[g_{ij}^{\text{target}}(r)]$. Here, $g_{ij}^{\text{target}}(r)$ is the pair distribution function between different solvent components obtained from the reference all-atom simulation. Then the potentials are updated over several iterations n using the protocol, $V_n^{\text{IBI}}(r) = V_{n-1}^{\text{IBI}}(r) + k_B T \ln[g_{ij}^{n-1}(r)/g_{ij}^{\text{target}}(r)]$. Furthermore, in the IBI protocol, solution component fluctuations that are related to the tail of $g_{ij}(r)$ sometimes need fine-tuning, especially when dealing with multicomponent systems. For this purpose, the C-IBI might serve as a possible candidate. In C-IBI, the initial guess of potential is taken from IBI, i.e., $V_n^{\text{IBI}}(r)$, which is then updated with a protocol, $V_{n+1}^{\text{C-IBI}}(r) = V_n^{\text{C-IBI}}(r) + k_B T \ln[C_{ij}^n(r)/C_{ij}^{\text{target}}(r)]$, with cumulative integral $C_{ij}^n(r) = 4\pi \int_0^r g_{ij}^n(r') r'^2 dr'$. Here, a single set of CG potentials (see **Figure 4d**), obtained from the monomer-level simulations of individual monomer species, could explain a broad range of copolymer sequence (80) synthesized experimentally (13; see **Table 1**). This makes the CG model obtained from a structure-based CG method sequence transferable (80). In addition, these simulations were performed with exactly the same molecular weights as those in experiments, i.e., $M_n \approx 10^4$ g/mol.

2.2.1. Extension of coarse-grained model for amphiphilic bottle brush polymers. A simple CG model, like the one discussed above, can also effectively capture the solution behavior of other polymer architectures (such as the bottle brush polymers) consisting of alkane backbone and ethylene oxide side chains (85). In this context, it was experimentally shown that though a single bottle brush polymer consisting of the ethylene oxide side chain and the alkane backbone is well soluble in aqueous solutions in semidilute concentration these polymers form large aggregates. As elucidated by the all-atom simulations (see simulation snapshot in **Figure 5a**), these bottle brush systems can self-assemble in their semidilute solution. These aggregates are due to the

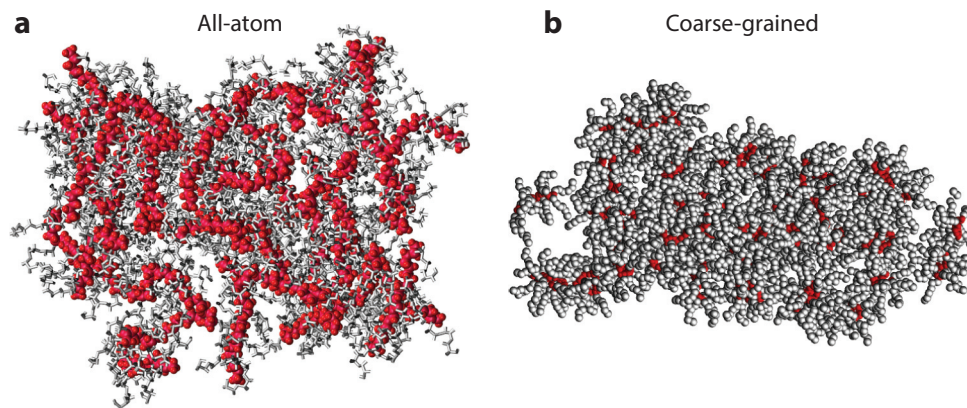
Table 1 Copolymer conformations with different sequences n_1 , m_1 , n_2 , and m_2 ^a

n_1	m_1	n_2	m_2	Experiment (13)	Simulation (80)
4	0	2	1	Turbid	Globule
4	0	2	2	Turbid	Globule
4	0	2	3	Turbid	Globule
2	1	2	1	Turbid	Globule
2	1	2	2	Turbid	Globule
2	1	2	3	Clear	Lamellar
2	2	2	1	Clear	Globule
2	2	2	2	Clear	Expanded
2	2	2	3	Clear	Expanded

^aIn the last two columns, comparisons of polymer conformation from experiments and CG simulations are shown. Note: Experiments were performed around the semidilute regime, and simulation data are shown for single chain limit. Therefore, turbid solution corresponds to collapsed object and clear solution shows good solubility, i.e., expanded chain conformation (80).

interdigitation of ethylene oxide side chains that originate owing to attraction between hydrophobic $-\text{CH}_2$ patches within the side chains. More interestingly, the CG potential obtained in **Figure 4d** can reproduce well the aggregation behavior of the bottle brush polymer (see **Figure 5b**). Note that in the CG model molecular weights of polymer chains are exactly the same as they are in the experimental system (85).

2.2.2. Temperature transferability of the coarse-grained model. The CG model described above was derived for individual monomers and was used to describe a broad range of copolymer sequences, thus making it a sequence transferable model. However, this model can only be applied at a particular T . For example, structure-based CG methods are dependent on pair-wise structures that inherently depend on temperature, thus making structure-based CG models

**Figure 5**

Simulation snapshot showing aggregation of bottle brush polymer consisting of alkane backbone and ethylene oxide side chains. A comparison of (a) all-atom and (b) CG simulation results are shown. The molecular weight M_n for all-atom simulations were half the M_n from experimental synthesis. For CG simulation, M_n is the same as experimental polymers. Abbreviation: CG, coarse-grained. Figure adapted with permission from *ACS Macro Letters* 6, 241; Copyright 2017 American Chemical Society.

state-point dependent and not transferable with changing T . A recent work derived a CG model for a PNIPAm chain in bundled water (four water molecules clustered into one CG bead) (86) based on the CG force field (87, 88). This work presented results for two different temperatures, in which two different sets of pair-wise CG potentials were used to account for the temperature effect (86). Furthermore, when a polymer undergoes coil-to-globule transition, it is dictated by a delicate balance between entropy and energy near the transition point that originates from the three-body effects. It should still be mentioned that CG potentials are free energies when compared with the all-atom models, thus they are linked to a thermodynamic state point and one cannot expect temperature transferability. However, if a CG model can properly account for this delicate entropy–energy balance, as in the case of azobenzene (89), it is expected that the underlying CG model may also be temperature transferable.

3. CO-NON-SOLVENCY: POLYMER COLLAPSE IN MISCIBLE GOOD SOLVENTS

So far, we have discussed polymer properties in single-component solvents and their coil-to-globule transition with change in temperature. However, the conformational behavior of a polymer can also be greatly influenced by the presence of small cosolvent molecules within the solvation volume of a polymer in solution. This leads to competitive interactions of solvents and cosolvents with a polymer. This is because cosolvents can often drastically alter the solvation structure and, thus, the solvation free energy of a polymer (18–20, 24, 26). For example, starting from an expanded chain of PNIPAm in pure water below its T_ℓ , addition of cosolvent (especially small alcohols and other organic solvents) first decreases T_ℓ , and then T_ℓ eventually sharply increases when alcohol content increases beyond a certain concentration (18, 19). In **Figure 6**, a representative phase diagram of PNIPAm in aqueous methanol mixture is shown. This phase diagram clearly indicates that, for a given temperature (lets say the room temperature 298 K), increasing molar cosolvent concentration x_c (in this case alcohol) first causes the chain to collapse and then to expand again, when x_c is increased above a critical value. This coil-globule-coil transition is referred to as co-non-solvency. Interestingly, even when the co-non-solvency of PNIPAm was reported in 1991 (18, 19), the term co-non-solvency was already coined in 1978 to describe the solvation of polystyrene in a mixture of cyclohexane-dimethylformamide (cyclohexane-DMF) solution (90). It should also be highlighted that water and short alcohols (such as methanol and ethanol) are well miscible over the full water–alcohol mixing ratios. Furthermore, larger alcohols (such as propanol and butanol) become less and less soluble in water. Here, if the bulk solvent–cosolvent solution was phase separated, it would be obvious to explain the phenomenon of co-non-solvency. For example, in a phase-separated binary mixture a polymer would prefer to sit in the interfacial region between two solvents because of the reduced interfacial tension and, thus, a chain remains expanded within the interface. Increasing polymer concentration would then lead to polymer collapse because of polymer crowding. In this case, however, a single chain would not show a coil-to-globule transition (32). However, if both solvents were strongly attractive compared with monomer–solvent or monomer–cosolvent interactions, one would expect to have a polymer falling out of solution driving the phase separation (91, 92). It should be mentioned, however, that the common solvent mixtures, where co-non-solvency is observed, are fairly miscible (but not perfectly miscible), as in the case of water and alcohol. Data that somewhat demonstrate this are the density variation of aqueous alcohol solution with changing relative mixing ratios; i.e., total number density reduces from the mean-field value with a minima around 50–50 mixing. This is due to rather weak steric repulsion between two components (93).

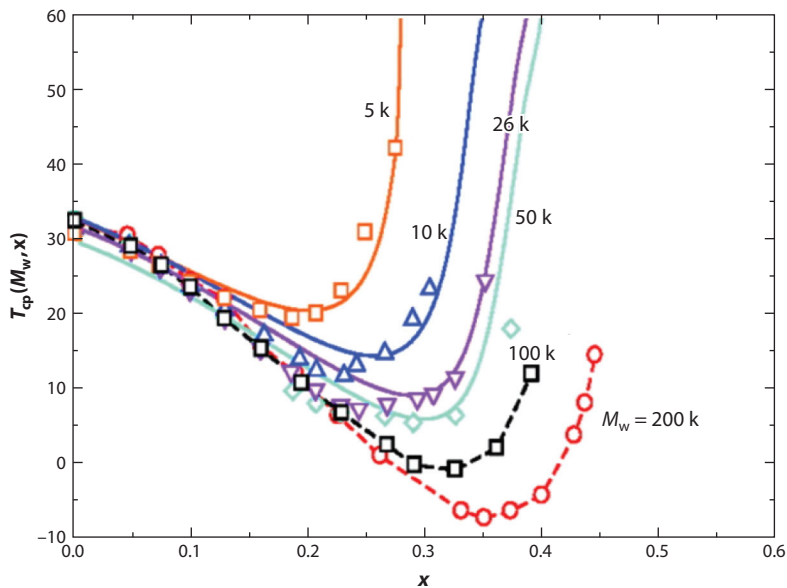


Figure 6

Lower critical solution temperature of poly(N-isopropylacrylamide) in aqueous methanol mixture for different methanol concentrations. Data are shown for different polymer molecular weights. The higher the molecular weight, the broader the window of collapse. The region above the phase lines shows phase-separated (two-phase) system, whereas the miscible region is below the phase line. Figure adapted with permission from *Macromolecules* 44, 2978; Copyright 2011 American Chemical Society.

What causes co-non-solvency in fairly miscible binary mixtures? More specifically, we need to understand factors that cause a decrease in T_c with increasing cosolvent concentration while noting that the original temperature-driven collapse of a chain in water is entropy driven. Extensive studies—experiments, theory, and computer simulations—have been conducted, but this puzzling behavior is still under debate. In view of the above explanations, three main pictures were proposed as the microscopic origin of co-non-solvency; they are based on solvent–cosolvent interactions (18, 32, 91, 92), cooperative polymer–solvent and polymer–cosolvent hydrogen bonding (24, 26), and preferential polymer–cosolvent binding (28–30). Therefore, we proceed here with highlighting results from the molecular simulations.

3.1. Multiscale Simulations, Complex Mixtures, and Polymer in Mixed Solvents

As mentioned earlier, polymer properties are governed by a rather delicate energy (details of the chemical structure) and entropy (generic, universal scaling laws, critical phenomena) interplay. This connection is at the heart of the understanding of many biological as well as synthetic materials and processes. At the same time, it is difficult to link microscopic details with the materials properties within conventional experimental and mid-sized canonical (NVT) or isobaric (NpT) simulation setups, where N is the number of particles in the simulation box, V is volume of the system, T is the temperature, and p is the pressure. Therefore, there is a need to address these problems within multiscale simulation approaches, in which local microscopic interaction details (where local is referred to as the range of correlation length that is typically less than 2.0 nm in these water soluble systems) are coupled in equilibrium with a large solvent bath allowing for global conformational fluctuations. For example, polymer properties in mixed solvents typically are

dictated by large conformational and (co-)solvent compositional fluctuations. Computer simulations in canonical ensemble usually, however, suffer from system size effects (94, 95). This is partially because the local aggregation of one of the solvent components at one place of a simulation box leads to the depletion of the same species at a different region within the simulation box. This disturbs the solvent equilibrium and affects the relative density fluctuations, especially for the small- to mid-sized simulation domains.

A quantity that gives the direct measure of the fluctuations within the simulation domain is

$$G_{ij} = 4\pi \int_0^\infty \left[g_{ij}^{\mu VT}(r) - 1 \right] r^2 dr = V \left[\frac{\langle N_i N_j \rangle - \langle N_i \rangle \langle N_j \rangle}{\langle N_i \rangle \langle N_j \rangle} - \frac{\delta_{ij}}{\langle N_j \rangle} \right], \quad 2.$$

where thermal averages are denoted by brackets $\langle \cdot \rangle$. V is the volume, N_i is the number of particles of species i , δ_{ij} is the Kronecker delta, $g_{ij}^{\mu VT}(r)$ is the radial distribution function in the μVT ensemble (30, 95–99). Here, G_{ij} is referred differently in different communities. In the bio-physical community G_{ij} is known as the Kirkwood–Buff integral (KBI; 96) and in statistical physics $G_{ij}/4\pi$ is known as the Mayer’s function. Here, $-G_{ij}/2$ also gives a direct measure of the second virial coefficient β_2 (or the excluded volume \mathcal{V}), a highly useful quantity to describe polymer conformations (6, 29, 63–65). Furthermore, G_{ij} is a local quantity that can be used as a measure of the affinity between solution components i and j . A positive (or negative) value of G_{ij} refers to excess (or depletion) of component j around component i . G_{ij} can also be used to calculate solvation thermodynamics of multicomponent complex fluids.

Following Equation 2 G_{ij} should be calculated in a grand canonical ensemble, while in a closed boundary setup G_{ij} can only be estimated at $r \rightarrow \infty$ (96). Typical cumulative G_{ij} are shown in **Figure 7a**. For a small system size (consisting of 6×10^3 molecules), $G_{ij}(r)$ suffers from severe system size effects and it is impossible to get any reasonable converged value for G_{ij} , which can, however, be estimated from a 21,000 molecule system (30). This clearly demonstrates that a large

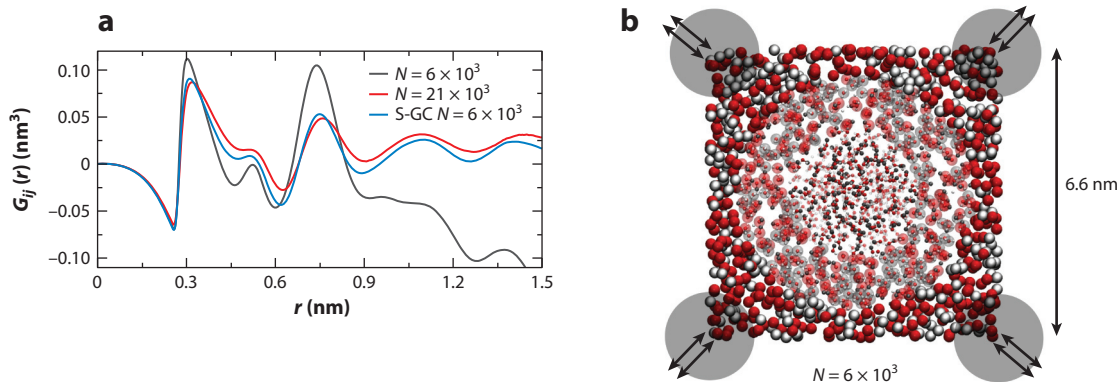


Figure 7

(a) Kirkwood–Buff integrals of an aqueous methanol mixture for the methanol mole fraction of $x_c = 0.90$. Results are shown for two different methods: all-atom simulations (red and black curves) and S-GC molecular dynamics (blue curve). Also for two different system sizes. (b) A schematic representation of the S-GC scheme with periodic boundary condition. Conventional AdResS is used, where a small AA region is coupled to a much smaller S-GC reservoir. The particle exchange is performed at the corners (gray shaded circles) keeping the constant chemical potential. The size of the AA is similar to the correlation length of the molecular liquid. Oxygen is shown in red, hydrogen in silver, and the united atom CH_3 is shown in steel. The red and silver beads represent methanol and water, respectively. Abbreviations: AA, all atom; AdResS, adaptive resolution scheme; S-GC, semi-grand canonical. Figure adapted with permission from *Macromolecules* 46, 9158; Copyright 2013 American Chemical Society.

system size is required to maintain solvent equilibrium and to avoid severe system size effects. In this context, because the original KB theory is derived in a μVT ensemble, it might be better to estimate these quantities within a grand canonical environment.

Implementation of grand canonical environment in a molecular simulation requires the introduction of particle insertion and deletion moves. Furthermore, in a molecular liquid, particle insertion suffers from poor acceptance rates (i.e., one acceptance out of a million attempts) because of significant particle overlap (100). Therefore, an alternative is to use a semi-grand canonical (S-GC) protocol, where particle identities are exchanged satisfying a Metropolis particle exchange criterion. For example, in a binary complex mixture, based on the chemical potential (or relative composition) of a particular solution, particle identity is switched between one species and the other. Even this also suffers from poor acceptance rates for an all-atom simulation. If instead molecules are represented by CG spheres, their exchange can be much easier.

S-GC molecular dynamics combines with an adaptive resolution scheme (AdResS) (101) with a particle exchange move. In AdResS, a high-resolution all-atom simulation domain is coupled with a low-resolution CG reservoir with periodic boundary conditions. Particle exchange is introduced in the CG reservoir. A schematic of the S-GC scheme is shown in **Figure 7b**. Particle exchange was performed at eight corners of the simulation domain. Using S-GC scheme, converged KBI can be obtained (see **Figure 7a**). Therefore, S-GC scheme guarantees solvent equilibrium and thus can be used to study complex conformational transition of large macromolecules. There is also a vast range of distinct methods to compute thermodynamic quantities from particle fluctuations in open boundary molecular simulations (30, 95–99).

Figure 8 shows gyration radius R_g as a function of methanol mole fraction x_c . Data are shown from S-GC simulations (**Figure 8a**) and a master curve (**Figure 8b**; 30). Furthermore, **Figure 8b** also shows data from generic simulations, experiments, and analytical theory. Note that detailed theory will be discussed in a later section. Here generic simulations are based only on the Lennard–Jones (LJ) interactions between different solution components that are tuned to reproduce correct solvation free energy known from all-atom simulations. Furthermore, for an atactic PNIPAm chain one has $\ell_p \sim 2.5$ – 3.0 monomers or $\ell_p \sim 1$ nm. In our generic simulations, one bead (of size 1σ) corresponds to 2.5–3.0 NIPAm monomers. This leads to a mapping of $1 \sigma \sim 1$ nm (102).

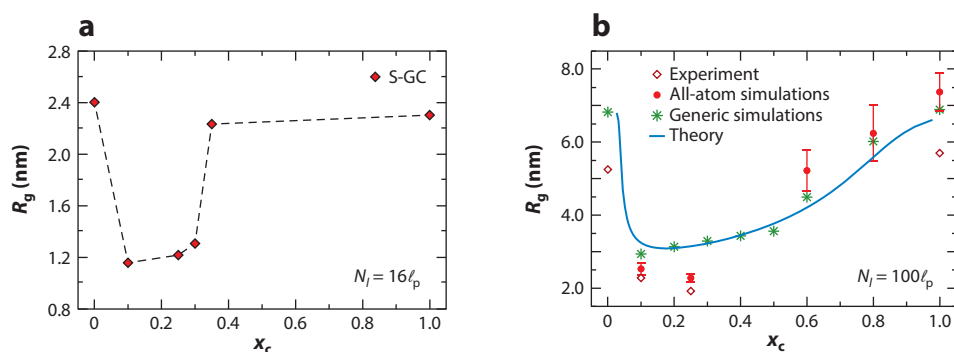


Figure 8

Gyration radius R_g as a function of cosolvent mole fraction x_c . (a) Results from S-GC molecular dynamics for a chain length of $N_l \sim 16\ell_p$, with ℓ_p being the persistence length. (b) A master curve of all-atom simulations, generic simulations, and experimental measurements for $N_l \sim 100\ell_p$. For comparison, analytical plot is also included for $N_l = 100\ell_p$. Abbreviation: S-GC, semi-grand canonical. Panel a adapted with permission from *Macromolecules* 46, 9158; Copyright 2013 American Chemical Society, and panel b adapted with permission from *Soft Matter* 12, 7995; Copyright 2016 Royal Society of Chemistry.

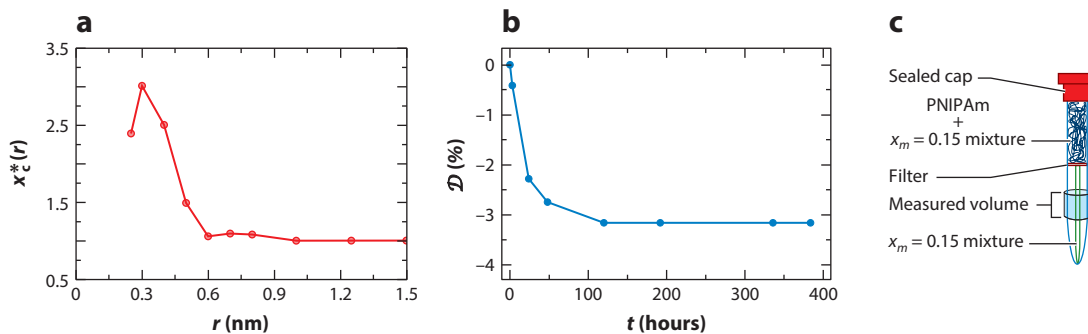


Figure 9

(a) Excess cosolvent mole fraction x_c^* as a function of radial distance r from the polymer backbone. (b) Proton NMR data showing solvent uptake by the upper panel of the NMR tube (panel c) containing polymer. Abbreviation: NMR, nuclear magnetic resonance. Figure adapted with permission from *Soft Matter* 12, 7995; Copyright 2016 Royal Society of Chemistry.

From **Figure 8** it can be appreciated that the generic features of coil-globule-coil behavior are observed in experiments (18–20), and all-atom (102), generic (3), and S-GC simulations (30). Another interesting observation from **Figure 8** is that the longer the chain, the broader the window of collapse as also observed earlier (26). Here, however, the goal of simulation is not only to reproduce experiments but also to provide a direct molecular level description of the mechanism governing properties of a physical system.

Whenever a polymeric system undergoes a conformational transition, it is associated with the modification of solvent structure within the solvation volume of the polymer. In **Figure 9a** the relative mole fraction of cosolvent x_c^* as a function of radial distance r from the polymer backbone with respect to the bulk solution cosolvent mole fraction $x_c = 0.1$ is shown (68, 103). In a nutshell, $x_c^* > 1$ shows an excess of cosolvent, while $x_c^* = 1$ shows the bulk solution mole fraction. It can be appreciated that within the first solvation shell (i.e., $r < 0.6$ nm) there is almost a three-fold increase in cosolvent composition, which is a result of cosolvent molecules replacing solvent because of their preferential binding with the polymer. To test this observation of preferential monomer–cosolvent interactions proton NMR measurements are shown in **Figure 9b** (102). During a measurement spanning over 16 days, composition of methanol was monitored in the lower panel of the NMR tube (see **Figure 9c**). As seen from **Figure 9b**, there is a reduction of about 3% alcohol in the lower panel of the tube, indicating that the concentrated polymer solution in the top panel attracts a significant amount of alcohol molecules. It should also be mentioned—even when 3% seems to be a rather small number, this is still significant considering that the volume of the lower panel in the NMR experiments is much larger than the top panel. Additionally, plateau in \mathcal{D} after four to five days also indicates that there is no solvent evaporation within the air-sealed NMR tube. It should be highlighted that earlier works also showed that the preferential monomer–cosolvent drives co-non-solvency (104, 105). A more recent work, however, also emphasized that the preferential monomer–cosolvent binding is not a prerequisite for co-non-solvency (106).

As it turned out, the preferential binding of one of the solvents to the polymer is driving the conformational transition of a polymer in mixed good solvents. This preferential binding is particularly important because if both solvents like polymers equally then only weak traces of nonideal mixing of the solvents are left, which are not sufficient to drive segregation. Furthermore, when one of the (co)solvents likes polymers more than the other, one can expect coil-globule-coil transition. Furthermore, this preferential binding is connected to very interesting thermodynamic

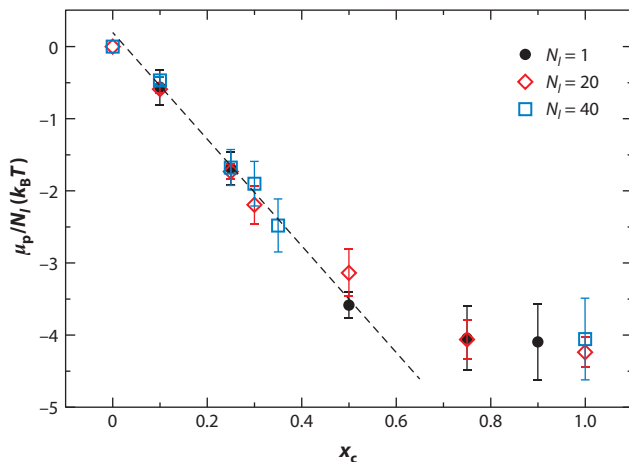


Figure 10

A master curve showing the shift in chemical potential μ_p per monomer as a function of cosolvent mole fraction. The data were obtained for a temperature of 298 K, where $k_B T = 2.5$ kJ/mol. Figure adapted with permission from *Macromolecules* 46, 9158; Copyright 2013 American Chemical Society.

properties (30). For example, in **Figure 10** the chemical potential of a polymer μ_p as a function of x_c is shown. μ_p monotonically decreases with increasing x_c , thus indicating that the solvation of polymer is becoming better-and-better with the increasing concentration of the better cosolvent. This is counterintuitive and puzzling, given that when a polymer goes from coil-to-globule transition it should get thermodynamically costlier to solvate a polymer, i.e., the solvent becomes a “poor” solvent. Here, we see strikingly different thermodynamic behavior. Therefore, within the simple thermodynamic arguments, co-non-solvency-based conformational transition would lead to low-high-low-type behavior of μ_p and not the ever decreasing solvation free energy, as seen in **Figure 10**. Therefore, there is a need to understand this phenomenon within theoretical framework.

3.2. Analytical Theory

The theoretical challenges posed by co-non-solvency were identified early on (18), as the first Flory–Huggins description of the observed collapsed was attempted. First theoretical progress was achieved later when more accurate theories for the LCST behavior of PNIPAM became available (24, 26). However, not until recently was the generic character of this phenomena recognized and explained by a combination of analytical theory and numerical simulations (3, 107).

3.2.1. Flory–Huggins mean-field theory. A standard thermodynamic theory to describe polymer conformation is the mean-field theory of Flory–Huggins. In this theory, when a polymer p with chain length N_l at volume fraction ϕ_p is dissolved in a binary mixture of solvent s and cosolvent c , the Flory–Huggins free energy \mathcal{F}_{FH} of polymer solutions is written as (63–65),

$$\begin{aligned} \frac{\mathcal{F}_{\text{FH}}}{k_B T} = & \frac{\phi_p}{N_l} \ln \phi_p + x_c (1 - \phi_p) \ln [x_c (1 - \phi_p)] + (1 - x_c) (1 - \phi_p) \ln [(1 - x_c) (1 - \phi_p)] \\ & + \chi_{ps} \phi_p (1 - x_c) (1 - \phi_p) + \chi_{pc} \phi_p x_c (1 - \phi_p) + \chi_{sc} x_c (1 - x_c) (1 - \phi_p)^2. \end{aligned} \quad 3.$$

Here, the first three terms represent the entropy of mixing and the last three terms deal with interactions between different components i and j through χ_{ij} parameters. The second-order expansion of Equation 3 gives a direct measure of the excluded volume \mathcal{V} of the polymer,

$$\mathcal{V} = 1 - 2(1 - x_c)\chi_{ps} - 2x_c\chi_{pc} + 2x_c(1 - x_c)\chi_{sc}, \quad 4.$$

In a nutshell, polymer conformations can be identified from their scaling laws of the static properties, especially from the gyration radius R_g and the single-chain static structure factor $S(q)$. Under good solvent conditions for a polymer, $\mathcal{V} > 0$ with $R_g \sim N_l^{3/5}$ and $S(q) \sim q^{-5/3}$. Increasing monomer–monomer attraction first brings a polymer into the Θ condition. At the Θ condition $\mathcal{V} = 0$, $R_g \sim N_l^{1/2}$ and $S(q) \sim q^{-2}$. When the monomer–monomer attraction is even further increased, a polymer collapses into a compact globule in which $\mathcal{V} < 0$, $R_g \sim N_l^{1/3}$, and $S(q) \sim q^{-4}$ (63–65).

When both solvent and cosolvent are good solvents for a polymer, $\chi_{ps} < 1/2$ and $\chi_{pc} < 1/2$ (18). If the bulk solution is perfectly miscible (i.e., $\chi_{sc} = 0$), the first two terms of Equation 4 give a linear variation of \mathcal{V} with x_c (**Figure 11a**). Only when $\chi_{sc} < 0$ can \mathcal{V} become negative, opening the possibility for the coil-to-globule-to-coil conformation changes typical of co-non-solvency (**Figure 11a**).

Furthermore, within the mean-field picture in Equation 3, the shift in chemical potential of polymer $\bar{\mu}_p$ under infinite dilution $\phi_p \rightarrow 0$ can be written as,

$$\begin{aligned} \bar{\mu}_p(\phi_p \rightarrow 0) &= \left. \frac{\partial \mathcal{F}_{\text{FH}}}{\partial \phi_p} \right|_{\phi_p \rightarrow 0} \\ &= \text{const} - x_c \ln x_c - (1 - x_c) \ln(1 - x_c) \\ &\quad + (1 - x_c)\chi_{ps} + x_c\chi_{pc} - 2x_c(1 - x_c)\chi_{sc}. \end{aligned} \quad 5.$$

In **Figure 11b** a schematic representation of $\bar{\mu}_p$ is shown as obtained from Equation 5. Note that $\bar{\mu}_p(x_c = 1) < \bar{\mu}_p(x_c = 0)$ because cosolvent is the better of the two (co)solvents. Furthermore the behavior of \mathcal{V} presented in **Figure 11** is consistent with the $\bar{\mu}_p$ for $\chi_{sc} < 0$ shown by a hump for

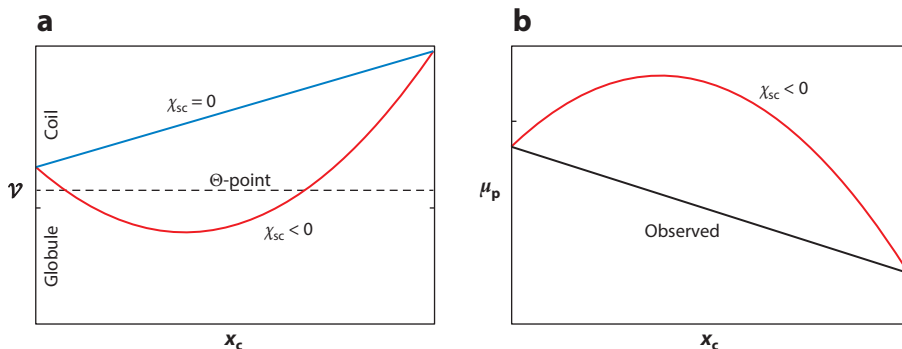


Figure 11

Schematic representations of the (a) polymer excluded volume \mathcal{V} and (b) chemical potential of polymer μ_p as functions of cosolvent mole fraction x_c . The dashed black line in panel a shows the Θ point when $\mathcal{V} = 0$. Figure adapted with permission from *Journal of Chemical Physics* 142, 114903; Copyright 2015 American Institute of Physics.

the intermediate mixing ratios, thus the solvent quality goes from good to poor to good again. We note that the trend in **Figure 10** is qualitatively different compared with that expected from the Flory–Huggins theory. In the mean-field picture, however, when $\chi_{sc} \gg 0$ a similar trend as that in **Figure 10** can be expected (see **Figure 11b**). Furthermore, this implies that the trend in $\bar{\mu}_p$ is obtained at the nonrealistic cost of driving the system towards solvent phase separation. In this context, it was already noticed early (18) that for common solvent mixtures where co-non-solvency effects are observed, such as water-alcohol mixtures, $\chi_{sc} \geq 0$.

3.2.2. Co-non-solvency as a result of cooperativity effects. A theoretical approach for describing the LCST behavior of PNIPAm was developed earlier (108), based on two central ideas: (a) water molecules bind to the PNIPAm backbone through hydrogen bonds, in a cooperative manner: the formation of bonds between one water molecule and the monomer facilitates the formation of the next bonds, and (b) the sections of the backbone without bound water molecules are naturally in a collapsed state while the sections with bound water molecules are naturally in good solvent conditions. An extension of this model for co-non-solvency was then considered (24) where both water and cosolvent were treated in the same manner, albeit with possible different values for the parameters measuring affinities and cooperativity. Model parameters could be found that fit very well experimental results on the variation of PNIPAm radius of gyration in water-methanol mixtures (24).

3.2.3. Competitive displacement of solvent by cosolvent. Although the approach in Reference 24 successfully displays the nonmonotonic collapse behavior of a polymer under co-non-solvency, it can lead to the conclusion that co-non-solvency can only be generated by the competition between two solvents that cooperatively bind to the chain backbone in a poor solvent. More recently it was shown that co-non-solvency is a generic phenomenon emerging in much less restrictive conditions.

As demonstrated by the simulations (see **Figure 9**), the polymer has preferential interactions with the cosolvent molecules. Because of this preferential interaction, when a small amount of cosolvents are added into the solution it tries to minimize the polymer-cosolvent binding free energy by attaching to more than one monomer at a time. Furthermore, the molecular flexibility of a polymer can help in this cause by forming segmental loops when cosolvent molecules form contact between two monomers far along the polymer backbone. Note that within the simplified generic model, one cosolvent sphere does not necessarily correspond to one alcohol molecule but rather a collection of several alcohol molecules.

The general picture of cosolvent molecules forming bridging interactions between two monomers topologically far along the polymer backbone has also been proposed for polymer collapse in a broad range of aqueous cosolvent mixtures. For example, the collapse of a PNIPAm in aqueous urea mixtures was shown to be driven by bridging-like hydrogen bonding of urea with two NIPAm monomers (15, 34). Furthermore, there are also other works showing that bridging interactions are responsible for a polymer collapse in a mixture of two cosolvents (35, 36), whereas another work highlighted that the preferential binding may not be prerequisite for co-non-solvency (106).

In view of this, a non-Flory–Huggins mean-field description of polymer solution can be formulated that is based on the Langmuir-like adsorption isotherm of competitive displacement (109). Within this theory, a polymer is considered to be an adsorbing substrate, where N sites are exposed to the bulk solution, of which n^s sites are occupied by s (solvent) molecules, n^c sites by nonbridging c (cosolvent) molecules, and $2n^b$ sites by bridging c (cosolvent) molecules, with $N = n^s + n^c + 2n^b$. The observed sequence of collapse and reswelling of the polymer corresponds to fast growth of

n_B^c as x_c increases, followed by displacement of n_B^c by n^c for larger x_c values. Such a sequence is typical for competitive displacement in adsorption phenomena (109).

The results from numerical simulations for n_B^c and n^c , or alternatively for the fractions $\phi_B = n_B^c/N$ and $\phi = n^c/N$, are well described by a competitive adsorption model with the following associated free-energy density of adsorption for nonbridges and bridges (3),

$$\begin{aligned} \frac{\Psi}{k_B T} = & \phi \ln(\phi) + \zeta \phi_B \ln(2\phi_B) + (1 - \phi - 2\phi_B) \ln(1 - \phi - 2\phi_B) \\ & - \mathcal{E}\phi - \mathcal{E}_B \phi_B - \frac{\mu}{k_B T} (\phi + \phi_B), \end{aligned} \quad 6.$$

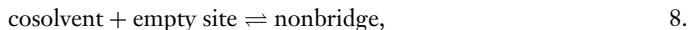
with $\mu = k_B T \ln(x_c)$ being the chemical potential of the cosolvent in the bulk solvent mixture and the adsorption energies \mathcal{E} and \mathcal{E}_B measuring the excess affinities of individual nonbridging and bridging cosolvent molecules to the chain monomers. The first three terms in Equation 6 express entropic contributions of the adsorbed bridges and nonbridges to the energy densities, whereas the two following terms measure contact energies between the cosolvents bridges and nonbridges with the polymer backbone. The unusual prefactor ζ is a consequence of assuming a logarithmic form for the dependence of the energy required to make a bridge on the average density of existing bridges. This is the case (3), for instance, if one assumes that in order to make a new bridge at density ϕ_B , the chain needs to make a loop of length $\ell = 1/\phi_B$, with associated penalty $\sim \log \ell \sim \log(1/\phi_B)$.

Minimization of Equation 6 with respect to ϕ_B and ϕ leads to the implicit equation for the bridge density $\phi_B(x_c)$,

$$16\phi_B^\zeta x_c = x_c^* \left\{ \left(\frac{x_c^*}{x_c^{**}} \right)^{1/2} (1 - 2\phi_B) \pm \sqrt{\left(\frac{x_c^*}{x_c^{**}} \right) (1 - 2\phi_B)^2 - 16\phi_B^\zeta} \right\}^2, \quad 7.$$

where $x_c^* = \exp(-\mathcal{E})$ and $x_c^{**} = \exp(-\mathcal{E}_B + 2 \ln 2e - \zeta)$ are the characteristic concentrations related to the adsorption energies \mathcal{E} and \mathcal{E}_B for nonbridges and bridges. In **Figure 12a**, we show ϕ_B as a function of x_c , which is well described by Equation 7 with $\zeta = 0.05$.

Equation 7 can equivalently be derived by considering the two pseudochemical reactions,



sketched in **Figure 13**. When the solvent and cosolvent interactions with the polymer backbone empty sites are described as pseudoreactions, a cosolvent molecule reacts with one empty adsorption site to form one adsorbed nonbridge, whereas it reacts with two empty sites to make ζ bridges. The associated equilibrium mass-action laws can thus be written as

$$\frac{x_c}{x_c^*} = \frac{\phi}{1 - \phi - 2\phi_B}, \quad 10.$$

$$\frac{x_c}{4x_c^{**}} = \frac{\phi_B^\zeta}{(1 - \phi - 2\phi_B)^2}, \quad 11.$$

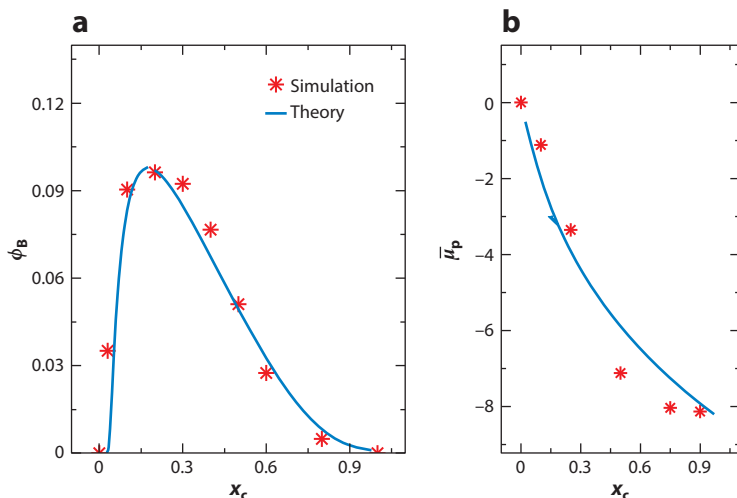


Figure 12

A comparative plot of molecular dynamics simulation (*symbols*) and theoretical plot (*solid line*). (*a*) Bridging fraction of cosolvents ϕ_B as a function of cosolvent mole fraction x_c . Theoretical prediction is represented by Equation 7. (*b*) Chemical potential shift $\bar{\mu}_p$ with x_c . Figure adapted with permission from *Journal of Chemical Physics* 142, 114903; Copyright 2015 American Institute of Physics.

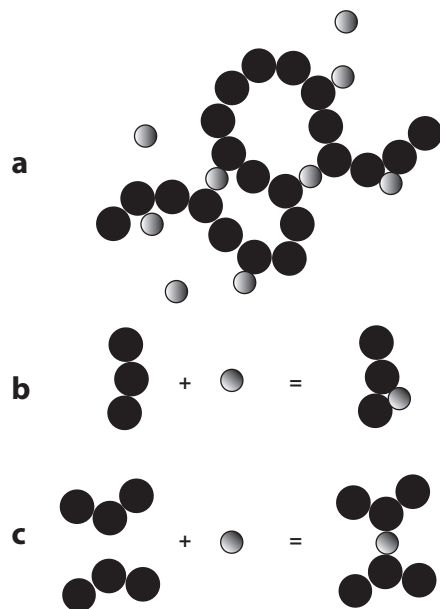


Figure 13

A schematic representation of the chemical reaction described in Equation 11. (*a*) A polymer conformation decorated by nonbridging and bridging cosolvents. Panel *b* shows a polymer segment and a cosolvent forming a single nonbridging cosolvent, whereas panel *c* represents two segments making a cosolvent bridge. Figure adapted with permission from *Journal of Chemical Physics* 142, 114903; Copyright 2015 American Institute of Physics.

with equilibrium reaction constants $1/x_c^*$ and $1/x_c^{**}$, where the reaction equilibrium concentration x_c^{**} has been, for mathematical convenience, defined up to a factor of four. Solving the mass-action laws for ϕ_B gives Equation 7. In this pseudochemical language, the factor ζ describing the effective number of bridges formed by the interaction between one cosolvent molecule and the two empty sites of the backbone appears as a consequence of assuming a power-law dependence for the equilibrium constant of the pseudochemical reaction. Note that the actual shape of Equation 7 is quite sensitive to the value of ζ . In particular, the choice $\zeta = 1$, corresponding to a standard chemical reaction between free species in solution, leads to a prediction that cannot describe our data.

In a previous work (3), it was argued that a value of $\zeta = 0.05$ can be understood by considering loop contributions to the cost of making a bridge. When a pure configurational cost for distributing the bridges among the possible occupation sites is combined with the entropic cost of loop formation, one can write $\zeta = 2 - m$. Here, the critical exponent m can be estimated within a simple scaling argument. In this context, one can characterize the loop formation by a partition function of vanishing end-to-end distance $R_e \rightarrow 0$ and $Z_{N_l}(R_e \rightarrow 0) \propto q^{N_l} N_l^{\alpha-2}$, and the partition function at finite R_e is given by $Z_{N_l}(R_e) \propto q^{N_l} N_l^{\gamma-1}$. Here, $1/q$ is the critical fugacity, and the universal exponent $\alpha \cong 0.2$ (65). From these two cases one can estimate the free-energy barrier to form a loop of length ℓ as $\Delta\mathcal{F}(\ell) = m k_B T \ln(\ell)$, with $m = \gamma - \alpha + 1$ being the critical exponent (65). Although this gives $m = 1.95$ for loop formation in self-avoiding walks, in excellent agreement with our findings, our simple analytical description does not address other possible contributions to bridge formation, such as the cooperative or other nontrivial entropic effects that might be determinant in the dense chain globule.

This selective adsorption model provides also for an analytical prediction of the shift in the chemical potential μ_p as a function of x_c ,

$$\frac{\mu_p}{k_B T} = \text{const} + (2 - \zeta) \phi_B - \ln \left[1 + \phi_B^{1-\zeta/2} \left(\frac{x_c}{x_c^{**}} \right)^{1/2} + \left(\frac{x_c}{x_c^{**}} \right) \right]. \quad 12.$$

Figure 12b shows a comparison between predictions from Equation 12 and the values of the chemical potential obtained from Equation 12. Good agreement is obtained by simply inserting into Equation 12 the values for ζ , and concentrations obtained from the fit of the bridging fraction shows validity of the approach (3).

Note that though standard Flory–Huggins-type mean-field theory does not describe co-non-solvency, mean-field descriptions with higher-order corrections may be more applicable. In this context, a recent extension of the competitive displacement concept (3, 107) led to the introduction of sticky sites within a mean-field picture to describe co-non-solvency of polymer brushes (110, 111).

3.3. Upper Critical Solution–Like Swelling of Lower Critical Solution Polymer

It is commonly known that a PNIPAm chain collapses in water upon increase of T , thus showing an LCST-like temperature effect. Furthermore, in aqueous alcohol mixtures, especially for larger alcohols (such as ethanol or propanol), PNIPAm also shows UCST-like swelling with increasing T (31, 68, 112). **Figure 14** shows that the UCST-like reswelling is more prominent for ethanol volume fraction $\phi_e > 50\%$ (68) for both simulation and experiments. This can be attributed to the fact that for $T > 305$ K pure water is always a poor solvent for PNIPAm, whereas no such LCST behavior is known for pure alcohol. Therefore, for $\phi_e > 50\%$, alcohol acts as an addition of good solvent in poor solvent, resulting in reswelling. Different studies have also explained this UCST-like swelling via kosmotropic effects (31) and cooperative hydrogen bonded effects (112).

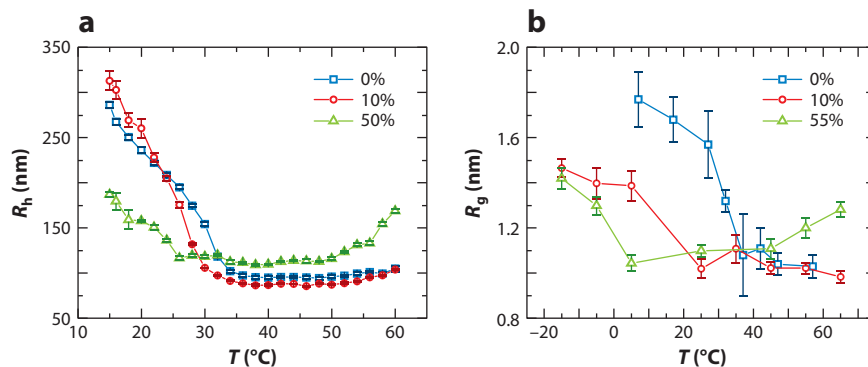


Figure 14

Hydrodynamic radius R_h obtained from (a) dynamics light scattering of PNIPAm microgel and (b) all-atom molecular dynamics simulations of a single PNIPAm chain. Data are shown from three different ethanol volume fractions and with varying temperature T . Abbreviation: PNIPAm, poly(N-isopropylacrylamide). Figure adapted with permission from *ACS Macro Letters* 6, 1042; Copyright 2017 American Chemical Society.

3.4. Elastin-Like Polypeptides in Aqueous and Aqueous Alcohol Mixtures

Another class of biocompatible LCST polymers is the elastin-like polypeptides (ELPs). ELPs are usually a five-amino-acid-based copolymer consisting of a sequence like Valine-Proline-Glycine-X-Glycine. Here, X can be any amino acid except Proline (9, 113, 114). These polymers often display a coil-to-globule transition with increasing temperatures, thus exhibiting an LCST transition. These synthetic polypeptides not only are fundamentally interesting but also offer a broad range of biotechnological applications. Recent experimental work reported that ELPs can exhibit co-non-solvency in aqueous alcohol mixtures (115). More interestingly, this study also reported a UCST-like expansion of ELP for high alcohol concentrations, as observed for PNIPAm (31, 68, 112).

4. CO-SOLVENCY: POLYMER SWELLING IN MISCIBLE POOR SOLVENTS

In the previous section, we reviewed the phenomenon of co-non-solvency that describes polymer collapse in a mixture of two competing, (fairly) miscible good solvents, whereas the same polymer remains expanded in these two solvents individually. An opposite phenomenon is that of the swelling of a polymer in mixtures of two fairly miscible poor solvents. In this context, it has been commonly observed that a polymer may remain collapsed in two different solvents, whereas it is somewhat better soluble in their mixtures (116–119). This phenomenon known as co-solvency is discussed in this section. Typical systems include poly(methyl methacrylate) (PMMA; 116–120), poly(N-(6-acetamidopyridin-2-yl)acrylamide) (PNAPAAm; 121), and corn starch in solvent mixtures (122). For example, PMMA is insoluble in both pure water and pure alcohol; it swells within the intermediate mixing ratios of water–alcohol mixtures (such as the aqueous methanol, ethanol, and propanol, respectively). A maximum degree of swelling around 60–70% alcohol mole fraction was attained as shown in **Figure 15**.

When a polymer collapses in a poor solvent, this collapsed structure is described by balancing negative second virial osmotic contributions $-|v|$ and three-body repulsions. Under such poor solvent conditions, the effective attraction between the monomers of a polymer can be viewed

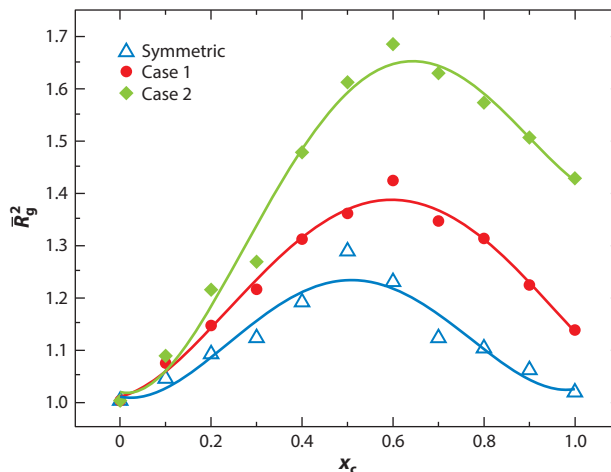


Figure 15

Normalized squared radius of gyration $\bar{R}_g^2 = \langle R_g^2 \rangle / \langle R_g(x_c = 0)^2 \rangle$ as a function of cosolvent molar concentration x_c . Results are shown for the generic simulations and for three different cases. Here, $\langle R_g(x_c = 0)^2 \rangle = 2.6 \pm 0.4\sigma^2$ and $\bar{R}_\Theta^2 = 2.13$, with $\bar{R}_\Theta = R_\Theta / R_g(x_c = 0)$ being the normalized Θ -point gyration radius. Here, case 2 closely mimics the conformational behavior of poly(methyl methacrylate) in aqueous methanol mixture. Figure adapted with permission from *Nature Communication* 8, 1374; Copyright 2017 Nature Publishing Group.

as a depletion-induced attraction, a phenomenon well described for colloidal suspensions (123–127) of purely repulsive particles. More specifically, monomer–monomer attraction occurs when monomer–solvent-excluded volume interactions become larger than the monomer–monomer-excluded volume interactions. The resulting isolated polymer conformation can be well described by the Porod scaling law of the single chain static structure factor $S(q) \propto q^{-4}$ presenting a compact spherical globule (see **Figure 16a**). This argument holds in pure water and in pure alcohol for PMMA. Furthermore, the extent of depletion-induced attraction between two particles is dictated by the number density ρ of depletants, in this case solvent particles consisting of water and alcohol within the solvation volume (6). Data that support this view are given by the total number density ρ_{total} of bulk solution as a function of mixing ratio of two solvents (6). **Figure 17** shows that for aqueous alcohol mixtures ρ_{total} reduces from its mean-field value (linear extrapolation between pure solvent $x_c = 0.0$ and pure cosolvent $x_c = 1.0$) with a maximum deviation observed for the 50–50 mixing ratio (93, 128). The larger the alcohol size ratio, the greater the deviation from the linear density of interpolation. This deviation is a key factor that reduces the number of depletants within the solvation volume and, thus, reduces the depletion-induced attractive forces, reducing the magnitude of the negative-excluded volume \mathcal{V} . Therefore, the polymer swelling in a mixture of two poor solvents can be viewed as a second-order effect. More specifically, the solvent molecules deplete monomers giving rise to the poor solvent condition for a polymer. However, when cosolvent molecules are added into the system, cosolvents deplete not only monomers but also solvent molecules, leading to a second-order depletion effect.

As discussed above, the mixed solvent remains a poor solvent, whereas the effective depletion that drives the polymer collapse is reduced. Thus, the observed swelling of about 30–70% in R_g^2 (or 10–30% swelling in R_g), as observed in **Figure 15**, does not mean that a polymer is fully swollen into a self-avoiding random walk. As seen from **Figure 16b**, $S(q)$ shows a crossover scaling: Within the range $1.5\sigma^{-1} < q < 3.0\sigma^{-1}$ an apparent scaling $S(q) \sim q^{-2}$ is observed, which crosses over to

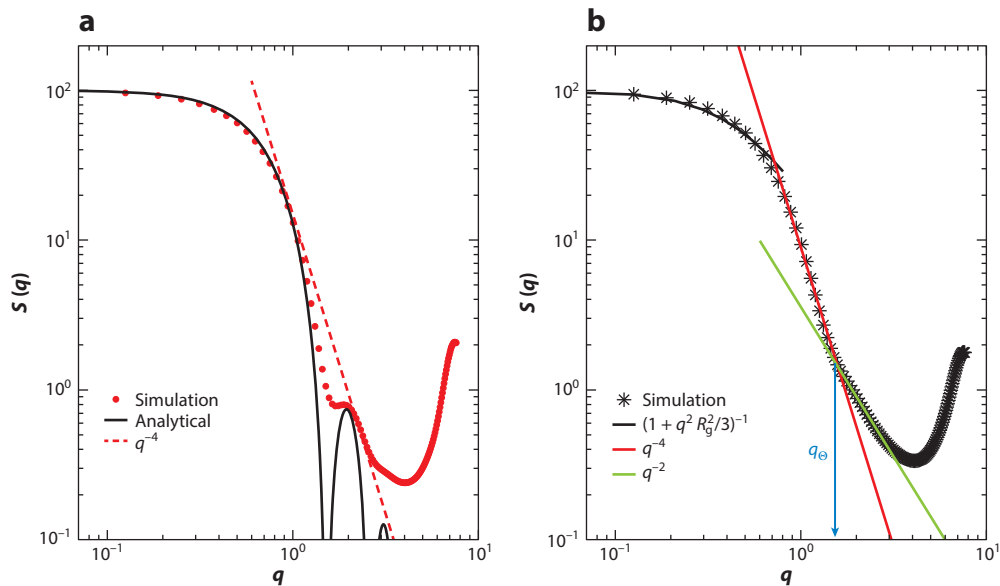


Figure 16

Single-chain static structure factor $S(q)$ for (a) $x_c = 0.0$ and (b) $x_c = 0.7$. In panel a, analytical expression for sphere scattering is included. In panel b, red and green lines are power-law fits to the data at different length scales. The black line represents the Guinier region for $q \rightarrow 0$. The vertical arrow indicates the effective Θ -like blob size at $q = q_\Theta$. Figure adapted with permission from *Nature Communication* 8, 1374; Copyright 2017 Nature Publishing Group.

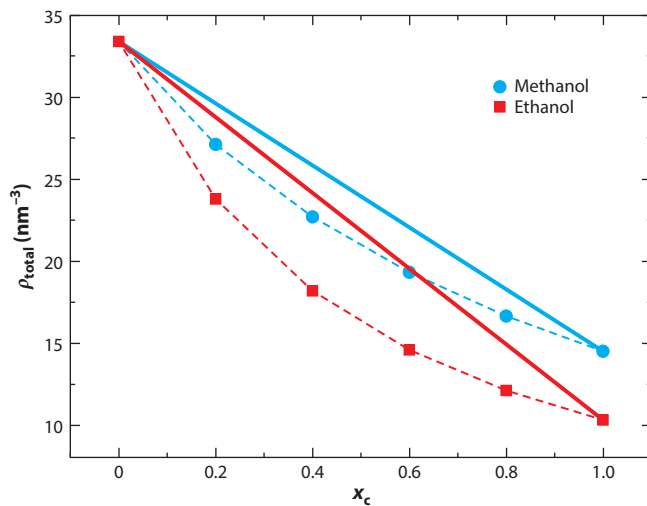


Figure 17

Total number density ρ_{total} of the bulk solution as a function of mole fraction x_c of aqueous methanol and aqueous ethanol solutions, respectively. Solid lines are linear interpolation between the data points of $x_c = 0.0$ and $x_c = 1.0$. Figure adapted with permission from *Journal of Physics Condensed Matter* 30, 024002; Copyright 2018 Institute of Physics.

$S(q) \sim q^{-4}$ for $0.7\sigma^{-1} < q < 1.5\sigma^{-1}$, suggesting that the polymer remains globally collapsed consisting of Θ -like blobs. The crossover point q_Θ gives the direct measure of the effective blob size $\ell_{\Theta\text{-blob}} = 2\pi/q_\Theta \sim 4.5\sigma$. The largest blobs are observed when the polymer is maximally swollen.

Unlike the phenomenon of co-non-solvency, which cannot be described within the standard Flory–Huggins-type mean-field theory, the phenomenon of co-solvency can be described within a Flory–Huggins picture. Furthermore, the bulk solvent–cosolvent interactions play an important role in describing the subtle co-solvency effect. For example, the density dip, as observed in **Figure 17**, is important for observing co-solvency. Here, it should also be emphasized that the density dip in ρ_{total} naturally emerges at constant pressures. In this context, a recent work has shown that the co-solvency can be explained within a unified picture combining the knowledge known from the polymer physics (63–65) and colloid science (123). Although a detailed theoretical analysis was presented in Reference 6 and somewhat in an earlier short review (128), we only sketch a few key ingredients here. For simplicity, a single chain at infinite dilution $\phi_p \rightarrow 0$ was considered, and most of the volume is occupied by solvent–cosolvent mixtures. Therefore, the system can be treated within a simplified limit of the binary mixture. In this case, the total free energy can be written as,

$$\frac{\mathcal{F}v}{k_B T} = \frac{v\mathcal{F}_s(v)}{k_B T} + x_c \ln(x_c) + (1 - x_c) \ln(1 - x_c) + \chi_{\text{sc}}(v)x_c(1 - x_c), \quad 13.$$

where $\mathcal{F}_s(v)$ is the volume-dependent free energy of the pure solvent of pure cosolvent systems. The Flory–Huggins interaction parameter χ_{sc} also depends on the system volume or solvent–cosolvent composition. For a given external pressure P , the molar volume v is thus controlled by,

$$P = P_s(v) - k_B T x_c(1 - x_c) \frac{\partial \chi_{\text{sc}}(v)}{\partial v}, \quad 14.$$

with $P_s(v) = -\partial v \mathcal{F}_s / \partial v$ being the pressure of the reference system. For a small variation of the molar volume of the solvent–cosolvent mixture with respect to that of the reference system, one gets $v = v_o [1 + \zeta x_c(1 - x_c)]$, where

$$\zeta = \frac{k_B T}{v} \frac{\partial \chi_{\text{sc}}(v)}{\partial v} \left[\frac{\partial P_s(v)}{\partial v} \right]^{-1} \quad 15.$$

measures the relative sensitivity of the interaction parameter and reference pressure to v . Furthermore, the change in χ_{sc} between constant density and constant pressure ensembles can be estimated from

$$\chi_{\text{sc}}(v) = \chi_{\text{sc}}(v_o) + v \frac{\partial \chi_{\text{sc}}(v)}{\partial v} \Big|_{x_c \rightarrow 0} \zeta x_c(1 - x_c). \quad 16.$$

Because $v \partial \chi_{\text{sc}}(v) / \partial v \sim \zeta$, this shows that χ_{sc} obtained between different ensembles is only perturbed to the second order in ζ . For $x_c = 0.5$, the above equation leads to an $\sim 11\%$ variation in χ_{sc} values with respect to the standard values calculated when ρ_{total} is kept constant (6). Even though 11% may sound like a small number, this is enough to induce polymer swelling in poor solvent mixtures. Note that in this case swelling does not mean a polymer undergoes a globule-to-coil transition but experiences a rather slight swelling as seen in **Figure 16**.

5. SMART POLYMERS FOR MATERIALS DESIGN

So far, we have emphasized the need to develop fundamental understanding of smart polymer properties in single and/or multicomponent solvents. Furthermore, polymers are ubiquitous in our everyday life, finding uses ranging from physics to materials science and from chemistry to biology (1, 4, 5). Therefore, discussions presented above also propose future directions for operational understanding and functional design principles of smart materials. For this purpose, molecular simulations are of particular importance in interpreting and guiding experiments in new directions. Therefore, we finish this review by sketching a few examples in which the knowledge discussed so far can be used to propose a design principle of polymeric materials.

5.1. Design of Multiresponsive Copolymer Architectures

In Section 2.2, a discussion is presented related to a sequence transferable CG model for polyacetal-based copolymer architectures (13, 80). Although varying parameter space with different sequences is rather nontrivial in experiments, the CG model can be used to predict a much broader range of polymer architectures. In **Figure 18**, a representative phase diagram for a broad range of polymer sequences is shown. Several interesting structures are observed reminiscent of the polysoap collapse (129–131).

Although conformations presented in **Figure 18** are shown for statistical copolymers, there are also studies predicting micellar structures of di- (or tri-)block copolymer architectures in pure water via thermal switching (11, 132–136). Furthermore, sometimes thermal switching requires a temperature change significantly above normal human body temperature. This often restricts broader applications of proposed polymer architectures for biomedical encapsulation. An alternative may, therefore, be to use ionic strengths (134, 136), tacticity (137), and co-solvent composition (33, 138) as switchable stimuli at a fixed T , preferably around ambient temperatures. Here, the phenomenon of co-non-solvency (see Section 3) can serve as an ideal

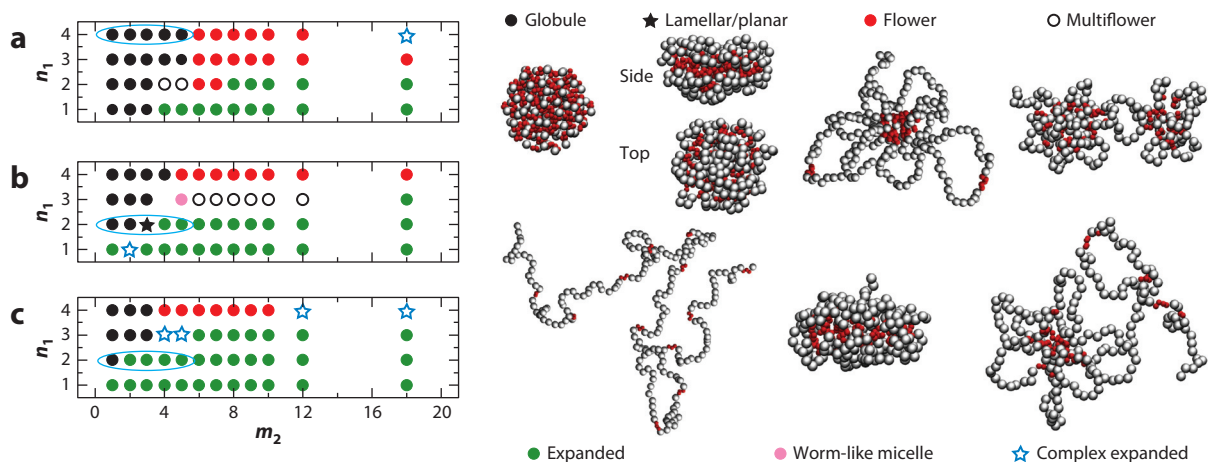


Figure 18

A representative phase diagram of the amphiphilic copolymers with different sequences; see **Figure 3**. Every symbol in this figure represents one configuration with the color code consistent with the configurations presented on the right. The data are shown for (a) $m_1 = 0$, (b) $m_1 = 1$, and (c) $m_1 = 2$ with $n_2 = 2$ and varying m_2 and n_1 . Ethylene oxide beads are rendered in silver and methylene units are represented by red spheres. Figure adapted with permission from *Journal of Chemical Physics* 147, 064904; Copyright 2017 American Institute of Physics.

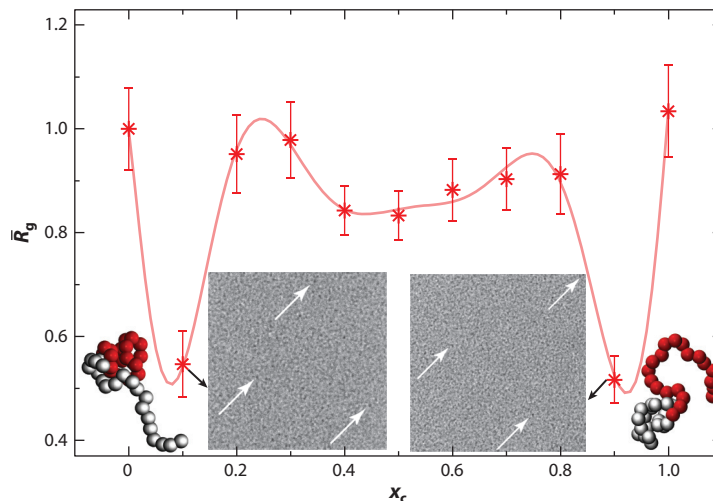


Figure 19

Main panel shows the normalized gyration radius $\bar{R}_g = R_g/R_g^0$ as a function of cosolvent mole fraction x_c obtained from generic molecular simulations. Two minima around $x_c = 0.1$ and 0.9 are because of the collapse of one block, as shown by the simulation snapshots. The inset also shows cryo-TEM images indicating the presence of micellar objects. Arrows in the cryo-TEM images indicate the region of maximum contrast. Abbreviation: TEM, transmission electron microscopy. Figure adapted with permission from *Macromolecules* 52, 3471; Copyright 2019 American Chemical Society.

platform to tune polymer conformation for a desired application. More specifically, if di-block copolymer architectures are designed such that different monomer units of a chain show distinct responsiveness in the same solvent–cosolvent mixtures (67, 138, 139), one can expect to see interesting structures. One possible example may be a di-block consisting of PNIPAm and poly(2-(methacryloyloxy)ethylphosphorycholine) (PMPC). The specific choice of these monomer structures is because both PNIPAm and PMPC show co-non-solvency in aqueous alcohol mixtures, whereas PNIPAm collapses at 10–40% and PMPC at 50–90% alcohol mixing ratios, respectively. A comparative figure showing conformation of a p(NIPAm-co-MPC) in aqueous ethanol mixtures is shown in **Figure 19**.

The generic molecular simulations predict a bimodal conformational transition (see the *main panel* of **Figure 19**), whereas cryo-TEM (cryo–transmission electron microscopy) also suggests micellar structures for $x_c = 0.1$ and 0.9 (see the *insets* in **Figure 19**). These interesting conformations show that solvent–cosolvent composition can induce switchable micellization.

5.2. Polymers with Improved Thermal Properties

Another interesting application of hydrogen-bonded polymers is their possible use for the tunable thermal properties of polymeric materials (54, 55, 140, 141). In typical nonmetallic crystals, lattice vibrations (or phonons) carry heat current, thus leading to very high κ values. Furthermore, in amorphous materials (as in the case of solid glassy polymers), phonon mean-free paths are vanishingly small and result in very low κ values. A simple theoretical model of thermal transport can, therefore, be obtained from the Einstein theory (142) incorporating the Debye model of vibrational states (143). This model, commonly referred to as the minimum thermal conductivity

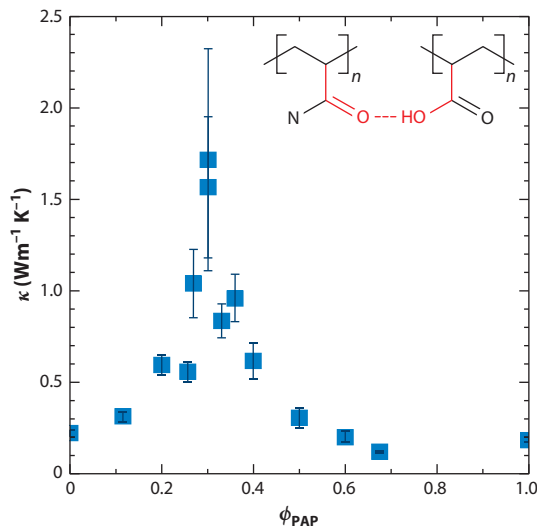


Figure 20

Thermal transport coefficient κ of PAA and PAP blend as a function of PAP monomer mole fractions ϕ_{PAP} . Abbreviations: PAA, poly(acrylic acid); PAP, poly(*N*-acryloyl piperidine). Figure adapted with permission from *Nature Materials* 14, 295; Copyright 2015 Nature Publishing Group.

model, suggests that $\kappa \propto v$ with v being the speed of sound wave; thus, they are also related to the material stiffness. In this context, though solid polymers are versatile and widely used, one drawback that often limits their usefulness under high-temperature conditions is their poor thermal conductivity κ . Most commonly known polymers, such as polystyrene, polypropylene, polycarbonate, and PMMA to name a few, show κ values that are below 0.2 W/K·m (140). κ of polymers can however be improved by blending them with high κ materials, such as the carbon-based materials that show κ exceeding above normal metals (144–147). Furthermore, significant improvement in κ often requires blending concentrations larger than their percolation threshold. A more attractive protocol, therefore, is to use monomer chemistry that shows stronger interaction between monomer segments (54, 55). Here, water-soluble polymers are of particular importance, where the dominant interaction is hydrogen bonding, the strength of which ranges between 4 and 8 $k_{\text{B}}T$ depending on temperatures and dielectric constants of the medium.

There are extensive recent interests in studying thermal properties of water-soluble polymers in their dry states (54, 55). This reaches from the homopolymer to copolymers and to polymer blends. For example, hydrogen-bonded homopolymer systems show $\kappa \sim 0.4$ W/K·m (55). In particular, when two hydrogen-bonded polymers are blended in, κ could be tuned with their typical values exceeding 1.5 W/K·m (54). One of the experimentally relevant systems is the asymmetric blend of a long poly(acrylic acid) (PAA) and a short poly(*N*-acryloyl piperidine) (PAP; see **Figure 20**). In another experimental study, a detailed investigation was conducted for a broad range of water-soluble polymers and polymer blends, where a less prominent variation of κ was observed for polymer blends (55). A more recent simulation study has investigated the links between morphology, materials stiffness, and κ for hydrogen-bonded systems (148), confirming experimental observation (55).

6. SUMMARY

Over the past three decades, the field of smart polymer research has grown enormously, and there is now an exciting body of literature about this class of polymers. In this short overview, we reviewed a facet of smart polymer research related to the solvation thermodynamics of hydrogen-bonded polymers in mostly aqueous mixtures. In particular, we discussed two symmetric, yet distinct, phenomena of polymers in miscible solvent mixtures: co-non-solvency and co-solvency. We have put these phenomena into perspective by a combination of multiscale modeling with complimentary experiments and analytical theories. Changes in solution behavior or morphology of polymer systems emerge as a function of external driving forces, such as the changes in temperature, concentration, or additives, and are subject to (small) chemical variations. We highlighted here the more recent unified frameworks that allow researchers to combine different concepts in order to arrive at tailor-made properties and materials design.

DISCLOSURE STATEMENT

The authors are not aware of any affiliations, memberships, funding, or financial holdings that might be perceived as affecting the objectivity of this review.

ACKNOWLEDGMENTS

We have reviewed several results that were obtained within fruitful collaborations with many colleagues, especially with Torsten Stühn, Paulo Netz, Tiago Oliveira, Manfred Wagner, Mark Watson, Marc Schmutz, Svenja Morsbach, Takahiro Ohkuma, Chaturanga De Silva, Porakrit Leophairatana, Jeffrey Koberstein, Sebastian Backes, Regine von Klitzing, David Ng, Tanja Weil, Daniel Bruns, and Jörg Rottler, and we take this opportunity to gratefully acknowledge them. Furthermore, this body of work has greatly benefited from stimulating discussions with Burkhard Dünweg, Martin Müser, Kostas Ch. Daoulas, and Robinson Cortes-Huerto. K.K. acknowledges the support by the European Research Council under the European Union's Seventh Framework Programme (FP7/2007-2013)/ERC Grant Agreement No. 340906-MOLPROCOMP. We further thank Robinson Cortes-Huerto and Tapan Chandra Adhyapak for their critical reading of this manuscript.

LITERATURE CITED

1. Cohen-Stuart MA, Huck WTS, Genzer J, Müller M, Ober C, et al. 2010. *Nat. Mater.* 9:101–13
2. de Beer S, Kutnyanszky E, Schön PM, Vancso GJ, Müser MH. 2014. *Nat. Commun.* 5:3781
3. Mukherji D, Marques CM, Kremer K. 2014. *Nat. Commun.* 5:4882
4. Halperin A, Kröger M, Winnik FM. 2015. *Angew. Chem. Int. Ed.* 54:15342–67
5. Zhang Q, Hoogenboom R. 2015. *Prog. Polym. Sci.* 48:122–42
6. Mukherji D, Marques CM, Stühn T, Kremer K. 2017. *Nat. Commun.* 8:1374
7. Wu C, Wang X. 1998. *Phys. Rev. Lett.* 80:4092–94
8. Wang X, Qui X, Wu C. 1998. *Macromolecules* 31:2972–76
9. Meyer DE, Chilkoti A. 1999. *Nat. Biotechnol.* 17:1112–15
10. Li C, Buurma NJ, Haq I, Turner C, Armes SP, et al. 2005. *Langmuir* 21:11026–33
11. Lutz JF, Akbemis Ö, Hoth A. 2006. *J. Am. Chem. Soc.* 128:13046–47
12. Cui S, Pang X, Zhang S, Yu Y, Ma H, Zhang X. 2012. *Langmuir* 28:5151–57
13. Samanta S, Bogdanowicz DR, Lu HH, Koberstein JT. 2016. *Macromolecules* 49:1858–64
14. Zhang M, Jia Y-G, Liu L, Li J, Zhu XX. 2018. *ACS Omega* 3:10172–79
15. Zhang Y, Furyk S, Bergbreiter DE, Cremer PS. 2005. *J. Am. Chem. Soc.* 127:14505–10
16. Sakota K, Tabata D, Sekiya H. 2015. *J. Phys. Chem. B* 119:10334–40

17. Okur HI, Hladilkova J, Rembert KB, Cho Y, Heyda J, et al. 2017. *J. Phys. Chem. B* 121:1997–2014
18. Schild HG, Muthukumar M, Tirrell DA. 1991. *Macromolecules* 24:948–52
19. Winnik FM, Ringsdorf H, Venzmer J. 1990. *Macromolecules* 23:2415–16
20. Zhang G, Wu C. 2001. *Phys. Rev. Lett.* 86:822–25
21. Hiroki A, Maekawa Y, Yoshida M, Kubota K, Katakai R. 2001. *Polymer* 42:1863–67
22. Kiritoshi Y, Ishihara K. 2002. *J. Biomater. Sci. Polym. Ed.* 13:213–24
23. Kiritoshi Y, Ishihara K. 2003. *Sci. Technol. Adv. Mater.* 4:93–98
24. Tanaka F, Koga T, Winnik FM. 2008. *Phys. Rev. Lett.* 101:028302
25. Sagle LB, Zhang Y, Litosh VA, Chen X, Cho Y, Cremer PS. 2010. *J. Am. Chem. Soc.* 131:9304–10
26. Tanaka F, Koga T, Kojima H, Xue N, Winnik FM. 2011. *Macromolecules* 44:2978–89
27. Kojima H, Tanaka F, Scherzinger C, Richtering W. 2012. *J. Polym. Sci. B* 51:1100–11
28. Walter J, Sehr J, Vrabec J, Hasse H. 2012. *J. Phys. Chem. B* 116:5251–59
29. Heyda J, Muzdalo A, Dzubiella J. 2013. *Macromolecules* 46:1231–38
30. Mukherji D, Kremer K. 2013. *Macromolecules* 46:9158–63
31. Bischofberger I, Calzolari DCE, Trappe V. 2014. *Soft Matter* 10:8288–95
32. Dudowicz J, Freed KF, Douglas JF. 2015. *J. Chem. Phys.* 143:131101
33. Kyriakos K, Philipp M, Lin C-H, Dyakonova M, Vishnevetskaya N, et al. 2016. *Macromol. Rapid Commun.* 37:420–25
34. Micciulla S, Michalowsky J, Schroer MA, Holm C, von Klitzing R, Smiatek J. 2016. *Phys. Chem. Chem. Phys.* 18:5324–35
35. Zhu P-W, Chen L. 2019. *Phys. Rev. E* 99:022501
36. Perez-Ramirez HA, Haro-Prez C, Vázquez-Contreras E, Klapp J, Bautista-Carbajald G, Odriozola G. 2019. *Phys. Chem. Chem. Phys.* 21:5106–16
37. Bédard MF, De Geest BG, Skirtach AG, Möhwald H, Sukhorukov GB. 2010. *Adv. Coll. Int. Sci.* 158(1–2):2–14
38. Ishii N, Obeid R, Qiu XP, Mamiya J, Ikeda T, Winnik FM. 2010. *Mol. Cryst. Liq. Cryst.* 529:60–70
39. Ishii N, Mamiya J, Ikeda T, Winnik FM. 2011. *Chem. Comm.* 47:1267–69
40. Esser-Kahn AP, Odom SA, Sottos NR, White SR, Moore JS. 2011. *Macromolecules* 44:5539–53
41. Zhao Y. 2012. *Macromolecules* 45:3647–57
42. Kitayama Y, Yoshikawa K, Takeuchi T. 2016. *Langmuir* 32:9245–53
43. Löwe C, Weber C. 2002. *Adv. Mat.* 14:1625–29
44. Caruso MM, Davis DA, Shen Q, Odom SA, Sottos NR, et al. 2009. *Chem. Rev.* 109:5755–98
45. Bruns N, Pustelny K, Bergeron LM, Whitehead TA, Clark DS. 2009. *Angew. Chem.* 48:5666–69
46. Hernandez-Sosa G, Bornemann N, Ringle I, Agari M, Dörsam E, et al. 2013. *Adv. Funct. Mater.* 23:3164–71
47. Yablonoitch E. 1987. *Phys. Rev. Lett.* 58:2059–62
48. John S. 1987. *Phys. Rev. Lett.* 58:2486–89
49. Fudouzi H, Xia Y. 2003. *Langmuir* 19:9653–60
50. Yin SN, Wang CF, Liu SS, Chen S. 2013. *J. Mater. Chem. C* 1:4685–92
51. Montarnal D, Capelot M, Tournilhac F, Leibler L. 2011. *Science* 334:965–68
52. Brutman JP, Delgado PA, Hillmyer MA. 2014. *ACS Macro Lett.* 3:607–10
53. Röttger M, Domenech T, van der Weegen R, Breuillac A, Nicolaÿ R, Leibler L. 2017. *Science* 356:62–65
54. Kim G, Lee D, Shanker A, Shao L, Kwon MS, et al. 2015. *Nat. Mater.* 14:295–300
55. Xie X, Li D, Tsai T, Liu J, Braun PV, Cahill DG. 2016. *Macromolecules* 49:972–78
56. Adams ML, Lavasanifar A, Kwon GS. 2003. *J. Pharm. Sci.* 92:1343–55
57. Chang DP, Dolbow JE, Zauscher S. 2007. *Langmuir* 23:250–57
58. Lee H, Lee BP, Messersmith PB. 2007. *Nature* 448:338–41
59. Batrakova EV, Kabanov AV. 2008. *J. Control Release* 130:98–106
60. Schmidt S, Zeiser M, Hellweg T, Duschl C, Fery A, Möhwald H. 2010. *Adv. Funct. Mater.* 20:3235–43
61. Vogel MJ, Steen PH. 2010. *PNAS* 107:3377–81
62. Meddahi-Pelle A, Legrand A, Marcellan A, Louedec L, Letourneur D, Leibler L. 2014. *Angew. Chem. Int. Ed.* 53:6369–73

63. de Gennes PG. 1979. *Scaling Concepts in Polymer Physics*. Ithaca, NY: Cornell Univ. Press
64. Doi M, Edwards SF. 1986. *The Theory of Polymer Dynamics*. Oxford, UK: Oxford University Press
65. Des Cloizeaux J, Jannink G. 1990. *Polymers in Solution: Their Modelling and Structure*. Oxford, UK: Clarendon
66. Kratz K, Hellweg T, Eimer W. 2000. *Coll. Surf. A: Phys. Eng. Aspects* 170:137–49
67. Scherzinger C, Lindner P, Keerl M, Richtering W. 2010. *Macromolecules* 43:6829–33
68. Backes S, Krause P, Tabaka W, Witt MU, Mukherji D, et al. 2017. *ACS Macro Lett.* 6:1042
69. Landau LD, Lifshitz EM. 2003. *Statistical Physics*. Amsterdam: Elsevier Butterworth-Heinemann. 3rd ed.
70. Jeppesen C, Kremer K. 1996. *Europhys. Lett.* 34:563–68
71. Kawasaki H, Nakamura T, Miyamoto K, Tokita M, Komai T. 1995. *J. Chem. Phys.* 103:6241–47
72. de Oliveira TE, Marques CM, Netz PA. 2018. *Phys. Chem. Chem. Phys.* 20:10100–7
73. Gernandt J, Frenning G, Richtering W, Hansson P. 2011. *Soft Matter* 7:10327–38
74. Ray B, Okamoto Y, Kamigaito M, Sawamoto M, Seno K, et al. 2005. *Polym. J.* 37:234–37
75. Hirano T, Okumura Y, Kitajima H, Seno M, Sato T. 2006. *J. Polym. Sci. A: Polym. Chem.* 44:4450–60
76. de Oliveira TE, Mukherji D, Kremer K, Netz PA. 2017. *J. Chem. Phys.* 146:034904
77. Hoffman AS, Stayton PS, Bulmus V, Chen G, Chen J, et al. 2000. *J. Biomed. Mater. Res.* 52:577–86
78. Shen Z, Terao K, Maki Y, Dobashi T, Ma G, Yamamoto T. 2006. *Colloid Polym. Sci.* 284:1001–7
79. Schulz B, Chudoba R, Heyda J, Dzubiella J. 2015. *J. Chem. Phys.* 143:243119
80. De Silva CC, Leophairatana P, Ohkuma T, Koberstein JT, Kremer K, Mukherji D. 2017. *J. Chem. Phys.* 147:064904
81. Tschöp W, Kremer K, Batoulis J, Bürger T, Hahn O. 1998. *Acta. Polym.* 49:61–74
82. Tschöp W, Kremer K, Batoulis J, Bürger T, Hahn O. 1998. *Acta. Polym.* 49:75–79
83. Reith D, Pütz M, Müller-Plathe F. 2003. *J. Comput. Chem.* 24:1624–36
84. de Oliveira TE, Netz PA, Kremer K, Junghans C, Mukherji D. 2016. *J. Chem. Phys.* 144:174106
85. Riegger A, Chen C, Zirafi O, Daiss N, Mukherji D, et al. 2017. *ACS Macro Lett.* 6:241–46
86. Abbott LJ, Stevens MJ. 2015. *J. Chem. Phys.* 143:244901
87. Shinoda W, DeVane R, Klein ML. 2007. *Mol. Simul.* 33:27–36
88. Marrink SJ, Tieleman DP. 2013. *Chem. Soc. Rev.* 42:6801–22
89. Mukherjee B, Delle Site L, Kremer K, Peter C. 2012. *J. Phys. Chem. B* 116:8474–84
90. Wolf BA, Willms MM. 1978. *Makromol. Chem.* 179:2265–77
91. Di J, Zuo T, Rogers S, Cheng H, Hammouda B, Han CC. 2016. *Macromolecules* 49:5152–59
92. Di J, Murugappan M, Cheng H, Han CC, Hammouda B. 2017. *Macromolecules* 50:7291–98
93. Perera A, Sokolic F, Almasy L, Koga Y. 2006. *J. Chem. Phys.* 124:124515
94. Mukherji D, van der Vegt NFA, Kremer K, Delle Site L. 2012. *J. Chem. Theor. Comp.* 8:375–79
95. Krüger P, Schnell SK, Bedeaux D, Kjølstrup S, Vlucht TJH, Simon JM. 2012. *J. Phys. Chem. Lett.* 4:235–38
96. Ben-Naim A. 2006. *Molecular Theory of Solutions*. Oxford, UK: Oxford Univ. Press
97. Cortes-Huerto R, Kremer K, Potestio R. 2016. *J. Chem. Phys.* 145:141103
98. Heidari M, Kremer K, Cortes-Huerto R, Potestio R. 2018. *J. Chem. Theor. Comp.* 14:3409–14
99. Panagiotis PC, Stefanos AD, Panagiotis-Nikolaos T, Theodorou DN. 2019. *J. Phys. Chem. B* 123:247–57
100. Frenkel D, Smit B. 2002. *Understanding Molecular Simulations*. New York: Academic. 2nd ed.
101. Praprotnik M, Delle Site L, Kremer K. 2005. *J. Chem. Phys.* 123:224106
102. Mukherji D, Wagner M, Watson MD, Winzen S, de Oliveir TE, et al. 2016. *Soft Matter* 12:7995–8003
103. Mukherji D, Kremer K. 2017. *Polym. Sci. Ser. C* 59:119–24
104. Magda JJ, Fredrickson GH, Larson RG, Helfand E. 1988. *Macromolecules* 21:726–32
105. Winnik FM, Ottaviani MF, Bossmann SH, Garcia-Garibay M, Turro NJ. 1992. *Macromolecules* 25:6007–17
106. Wang J, Wang N, Liu B, Bai J, Gong P, et al. 2017. *Phys. Chem. Chem. Phys.* 19:30097–106
107. Mukherji D, Marques CM, Stuehn T, Kremer K. 2015. *J. Chem. Phys.* 142:114903
108. Okada Y, Tanaka F. 2005. *Macromolecules* 38:4465–71
109. Hill TL. 1986. *An Introduction to Statistical Thermodynamics*. New York: Dover Publ.
110. Sommer JU. 2017. *Macromolecules* 50:2219–28

111. Sommer JU. 2018. *Macromolecules* 51:3066–74
112. Toshiki F, Shinyashiki N, Yagihara S, Kita R, Tanaka F. 2018. *Langmuir* 34:3003–9
113. Wu Y, Ng DYW, Kuan SL, Weil T. 2014. *Biomater. Sci.* 3:214–30
114. Weinberger A, Walter V, MacEwan SR, Schmatko T, Muller P, et al. 2017. *Sci. Rep.* 7:43963
115. Mills CE, Ding E, Olson BD. 2019. *Biomacromolecules* 6:2167–73
116. Masegosa RM, Prolongo MG, Hernandez-Feures I, Horta A. 1984. *Macromolecules* 17:1181–87
117. Hoogenboom R, Remzi BC, Guerrero-Sanchez C, Hoeppeener S, Schubert US. 2010. *Aust. J. Chem.* 63:1173–78
118. Lee SM, Bae YC. 2014. *Polymer* 55:4684–92
119. Yu Y, Kieviet BD, Kutnyansky E, Vancso GJ, de Beer S. 2015. *ACS Macro Lett.* 4:75–79
120. Wolf BA, Blaum GJ. 1975. *J. Polym. Sci. Polym. Phys. Ed.* 13:1115–32
121. Asadujjaman A, Ahmadi V, Yalcin M, ten Brummelhuis N, Bertin A. 2017. *Polym. Chem.* 8:3140–53
122. Galvez LO, de Beer S, van der Meer D, Pons A. 2017. *Phys. Rev. E* 95:030602
123. Lekkerkerker HNW, Tuinier R. 1990. *Colloids and the Depletion Interaction*. Oxford, UK: Clarendon
124. Mao Y, Cates ME, Lekkerkerker HNW. 1995. *Phys. Rev. Lett.* 75:4548–51
125. Mao Y, Cates ME, Lekkerkerker HNW. 1995. *Physica A* 222:10–24
126. Crocker JC, Matteo JA, Dinsmore AD, Yodh AG. 1999. *Phys. Rev. Lett.* 82:4352–55
127. Phillips R, et al. 2012. *Physical Biology of the Cell*. New York: Garland Sci. 2nd Ed.
128. Mukherji D, Marques CM, Kremer K. 2018. *J. Phys. Condens. Mat.* 30:024002
129. Borisov OV, Halperin A. 1995. *Langmuir* 11:2911–19
130. Lashewki A. 1995. *Adv. Polym. Sci.* 124:1–86
131. Lee NK, Abrams CF. 2004. *J. Chem. Phys.* 121:7484–93
132. Arotcarena M, Heise B, Ishaya S, Laschewsky A. 2002. *J. Am. Chem. Soc.* 124:3787–93
133. Chengming L, Buurma NJ, Haq I, Turner C, Armes SP, et al. 2005. *Langmuir* 21:11026–33
134. Vishnevetskaya NS, Hildebrand V, Niebuur BJ, Grillo I, Filippov SK, et al. 2017. *Macromolecules* 50:3985–99
135. Sezenenko T, Qiu XP, Winnik FM, Sato T. 2019. *Macromolecules* 52:935–44
136. Vishnevetskaya NS, Hildebrand V, Nizardo NM, Ko CH, Di Z, et al. 2019. *Langmuir* 35:6441–52
137. Hietala S, Nuopponen M, Kalliomaki K, Tenhu H. 2008. *Macromolecules* 41:2627–31
138. Mukherji D, Watson MD, Morsbach S, Schmutz M, Wagner M, et al. 2019. *Macromolecules* 52:3471–78
139. Kelley EG, Smart TP, Jackson AJ, Sullivana MO, Epps TH III. 2011. *Soft Matter* 7:7094–102
140. Choy CL. 1977. *Polymer* 18:984–1004
141. Shen S, Henry A, Tong J, Zheng R, Chen G. 2010. *Nat. Nanotech.* 5:251–55
142. Einstein A. 1911. *Ann. Phys.* 35:679–94
143. Cahill DG, Watson SK, Pohl RO. 1992. *Phys. Rev. B* 46:6131–40
144. Hu L, Desai T, Keblinski P. 2011. *J. App. Phys.* 110:033517
145. Pereira LFC, Donadio D. 2013. *Phys. Rev. B* 87:125424
146. Kodama T, Ohnishi M, Park W, Shiga T, Park J, et al. 2017. *Nat. Mat.* 16:892–97
147. Mahoney C, Hui CM, Majumdar S, Wang Z, Malen JA, et al. 2016. *Polymer* 93:72–77
148. Bruns D, de Oliveira TE, Rottler J, Mukherji D. 2019. *Macromolecules* 52:5510–17